
Expedition 315 methods¹

Expedition 315 Scientists²

Chapter contents

Introduction	1
X-ray computed tomography	3
Lithology	4
Structural geology	6
Biostratigraphy	10
Paleomagnetism	11
Inorganic geochemistry	14
Organic geochemistry	17
Microbiology	18
Physical properties	19
Core-log-seismic integration	23
References	24
Figures	27
Movies	50
Tables	52

Introduction

This chapter includes information on shipboard methods that will help the reader understand the basis for our preliminary interpretations and help the interested investigator select samples for further analysis.

Authorship of site chapters

The separate sections of the site chapters were written by the following shipboard scientists (authors are listed in alphabetical order; no seniority is implied):

Principal results: Expedition 315 Scientists
X-ray computed tomography: Lewis
Lithology: Calves, Guo, Hashimoto, Underwood
Structural geology: Behrmann, Byrne, Kanagawa, Lewis
Biostratigraphy: Boeckel, Hayashi
Paleomagnetism: Kanamatsu, Pares
Inorganic geochemistry: Hulme, Tomaru
Organic geochemistry: Saito
Microbiology: Kaksonen
Physical properties: Famin, Henry, Hirono, Kopf, Likos,
Schmidt-Schierhorn, Zhu
Core-log-seismic integration: Henry

Reference depths

Seafloor depths and cored intervals below seafloor (core depth below seafloor [CSF]) are determined by drill pipe measurement. When using Integrated Ocean Drilling Program (IODP) Method A, core expansion lengths overlap and are not scaled. We sometimes had more core recovery than coring advance (usually 9.5 m), especially in shallow sediments. These core lengths are linearly compressed to adjust to the coring advance and are labeled CSF-B to indicate core depth below seafloor calculated using IODP Method B (compression). Drilling engineers prefer to use pipe length to present the depth as drillers depth below rig floor (DRF). This measurement can be converted to CSF by subtracting water depth and the height of the rig floor from the sea surface. In some contexts referring to logging-while-drilling (LWD) results (as in “**Core-log-seismic integration**”), logging depths are presented as LWD depth below seafloor (LSF), which is also based on drill pipe measurement below seafloor.

¹Expedition 315 Scientists, 2009. Expedition 315 methods. In Kinoshita, M., Tobin, H., Ashi, J., Kimura, G., Lallemand, S., Sreaton, E.J., Curewitz, D., Masago, H., Moe, K.T., and the Expedition 314/315/316 Scientists, *Proc. IODP, 314/315/316*: Washington, DC (Integrated Ocean Drilling Program Management International, Inc.). doi:10.2204/iodp.proc.314315316.122.2009

²Expedition 314/315/316 Scientists' addresses.



Numbering of sites, holes, cores, sections, and samples

Sites drilled by the D/V *Chikyu* are numbered consecutively from the first site with a prefix “C.” A site refers to one or more holes drilled while the ship was positioned within 300 m of the first hole. The first hole drilled at a given site is assigned the site number modified by the suffix “A,” the second hole takes the site number and suffix “B,” and so forth. These suffixes are assigned regardless of recovery, as long as penetration takes place. During IODP Expedition 315, we drilled at Sites C0001 and C0002, both of which had been previously drilled during IODP Expedition 314. Therefore, hole names start with “E” for Site C0001 and “B” for Site C0002.

Each cored interval is generally 9.5 m long, which is the length of a core barrel. Coring intervals may be shorter and may not necessarily be adjacent if separated by intervals that were drilled but not cored. The core depth interval assigned to an individual core begins with the depth below seafloor at which the coring operation began and extends to the depth at which the coring operation ended for that core.

A recovered core is typically divided into 1.5 m long sections that are numbered serially from 1 beginning at the top. When the recovered core is shorter than the cored interval, the top of the core is equated with the top of the cored interval by convention in order to achieve consistency in handling analytical data derived from the cores. Also by convention, material recovered from the core catcher is placed in a separate section during core description, labeled core catcher (CC), and placed below the last (bottom) section recovered in the liner. The core catcher is placed at the top of the cored interval in cases where material is only recovered in the core catcher.

Samples removed from a core section are designated by distance measured in centimeters from the top of the section to the top and bottom of each sample removed from that section. A full identification number for a sample consists of the following information: expedition, site, hole, core number, core type, section number, and top to bottom interval in centimeters measured from the top of the section. For example, a sample identification of “315-C0001H-3R-2, 20–25 cm,” represents a sample removed from the interval between 20 and 25 cm below the top of Section 2. Core 3R designates that this core was taken using the rotary core barrel (RCB) in Hole C0001H during Expedition 315. All IODP core identifiers indicate core type. The following abbreviations are

used: H = hydraulic piston coring system (HPCS; equivalent to the advanced piston corer), X = extended shoe coring system (ESCS; equivalent to the extended core barrel), and R = RCB.

Core handling

As soon as a core is retrieved on deck, a sample is taken from the core catcher and, if sedimentary, sent to the paleontological laboratory for an initial age assessment. The Curator immediately measures the total length of the recovered core and informs the Wellsite Geologist. The Wellsite Geologist then registers the core number in the shipboard database J-CORES together with the drilling advance and other additional drilling information. The core liner with the core inside is marked into section lengths by the Curator, each section is numbered, and the core is cut into sections. Usually all of Section 4 is dedicated to interstitial water analyses. Therefore, Section 4 is frequently significantly shorter than 1.5 m. Its length varies from 20 to 45 cm depending on depth. This short section is immediately removed from the core cutting area and scanned with the X-ray computed tomography (CT) scanner to investigate internal structures in order to avoid losing unique tectonic or sedimentary features.

For safety monitoring, small (~5 cm³) plugs of sediment are taken from the bottom of Section 1 for headspace gas analysis. Each section is then sealed at the top and bottom with color-coded plastic caps and vinyl tape. A blue end cap marks the top of a section, a clear cap marks the bottom, and a yellow cap marks the end of a section from which a whole-round sample has been removed. The sample code (e.g., IW for interstitial water) is written on the yellow cap. Core sections are then carried into the laboratory, and the length of the core sections and any samples taken are logged into the J-CORES database.

In the laboratory, X-ray CT images are taken for all core sections. As mentioned above, a short section for interstitial water analysis is given top priority for X-ray CT scanning. A structural geologist and a sedimentologist examine section’s internal structures with real-time axial images to judge whether the section can be squeezed or not. If they find any important structures inside, the section is preserved and another whole-round sample candidate is taken for interstitial water analysis. Other sections are scanned with the X-ray CT in turn. After taking X-ray CT images, microbial whole-round samples are taken from a nonstructured less-disturbed horizon based on information gained from the X-ray CT images. Samples for anelastic strain recovery measurement are also taken at this time.

After core sections equilibrate to ambient room temperature (~3 h), they are run through the multisensor core logger (MSCL). For soft sediments, thermal conductivity measurements are then made (see “**Physical properties**”). After these nondestructive measurements, whole-round samples that are not time sensitive are taken. At the same time, 1 cm thick “cluster” slices are taken next to the whole-round sampling intervals. This thin round slice is divided into several pieces for different analytical purposes: X-ray diffraction (XRD; bulk), moisture and density (MAD), some organic chemistry analyses, and some shore-based analyses. This cluster sample provides a set of physical and chemical data for each sampling horizon, which enables more comprehensive geologic interpretation.

Cores are subsequently split lengthwise into working and archive halves. The archive half is used for non-destructive measurements: visual core description, paleomagnetism, digital photo image scanning, and color spectroscopy. Samples are taken from the working half for shipboard physical property measurements (see “**Physical properties**”) before being sampled for additional shipboard and postcruise studies. Finally, core sections are wrapped in plastic bags (heat shrink wrap) and transferred to cold-storage space aboard the drilling vessel. Following the expedition, cores are transported to the Kochi Core Center in Kochi, Japan.

X-ray computed tomography

X-ray CT imaging provided real-time constraints for Expedition 315 core logging and sampling strategies. The following explanation of our methods was derived from the “cookbook” prepared by CDEX/JAMSTEC for onboard use (X-Ray CT Scanner, version 3.00, 31 July 2007) and practical experience. The cookbook is based on GE Healthcare (2006), Mees et al. (2003), and Nakano et al. (2000).

The X-ray CT instrument on the *Chikyu* is a GE Yokogawa Medical Systems LightSpeed Ultra 16 capable of generating sixteen 0.625 mm thick slice images every 0.6 s, the time for one revolution of the X-ray source around the sample (see Table T1 for operating parameters). As a result of this high scanning rate, 1.5 m sections of core were typically imaged in <3 min. Data generated for each core consist of core-axis-normal planes of X-ray attenuation values with dimensions of 512 × 512 pixels. Data were stored as Digital Imaging and Communication in Medicine (DICOM) formatted files.

Background

The theory behind X-ray CT has been well established through medical research and is only briefly outlined here. X-ray intensity (I) varies as a function of X-ray path length and the linear attenuation coefficient (LAC) of the target material as

$$I = I_0 \times e^{-\mu L},$$

where

- I = transmitted X-ray intensity,
- I_0 = initial X-ray intensity,
- μ = LAC of the target material, and
- L = X-ray path length through the material.

LAC is a function of the chemical composition and density of the target material. The basic measure of attenuation, or radiodensity, is the CT number given in Hounsfield units (HU) and is defined as

$$\text{CT number} = [(\mu_t - \mu_w)/\mu_w] \times 1000,$$

where

- μ_t = LAC for the target material and
- μ_w = LAC for water.

The distribution of attenuation values mapped to an individual slice comprises the raw data that are used for subsequent image processing. Successive two-dimensional slices yield a representation of attenuation values in three-dimensional (3-D) pixels referred to as voxels. Visualizations are generally accomplished by varying the manner in which the distribution of CT number is assigned to 256 shades of gray or a color pallet. Onboard analysis of CT images was done primarily using the OsiriX 32-bit DICOM viewer (version 2.7.5) running on a G5 Macintosh (OS 10.4).

Analytical standards used during Expedition 315 were air (CT number = -1000), water (CT number = 0), and aluminum (2467 < CT number < 2487) in an acrylic core mock-up. The schedule for running these was fully implemented on 3 December 2007. All three standards were run once daily after air calibration, and once each week the three standards were run both before and after air calibration. For each standard analysis the CT number was determined for a 24.85 mm² area at fixed coordinates near the center of the cylinder (Table T2).

X-ray CT scan data usage

X-ray CT scans were used routinely during Expedition 315 to

- Provide an assessment of core and core-liner integrity,
- Determine the appropriateness of whole-round samples,
- Identify potentially subtle features and/or features that might warrant special handling during visual core description and sampling, and
- Measure orientations and identify crosscutting relationships.

CT scans provided first-hand information regarding the integrity of sample cores and core liners. Cores that experienced gas expulsion during depressurization could be readily identified (Fig. F1), as could cores in which extensive drilling-induced brecciation had occurred (Fig. F2). In several instances, core liners buckled into the sample along the core axis, displacing the sample, and in one case a liner partially delaminated and became entangled in a serpentine manner within the sample (Movie M1). CT scans also provided a fast and practical means of assessing the coherence of core intervals that contained abundant natural structures and were therefore targeted for additional paleomagnetic analyses.

All whole-round core sections were screened to avoid destructive testing on core samples that might contain critical structural features. This also ensured minimal drilling disturbance of whole-round samples (essential for microbiology as well as physical and mechanical properties) and an assessment of whole-round homogeneity. X-ray CT scanning was done immediately after core cutting so that time-sensitive whole-round samples (e.g., those for interstitial water and microbiological analyses) could be included in this screening process.

The value of X-ray CT scans to identify sedimentary and tectonic features prior to visual core description was quickly recognized (Movie M2). Three-dimensional structure orientation could easily be determined from CT sections, whereas performing the same measurement on the cores generally required cutting orthogonal faces. Furthermore, structures could be classified as a function of their CT contrast, which is presumably related to porosity changes or chemical alteration within shear zones. Observations were noted in the structural geology CT log sheets (Fig. F3) and are commonly referred to in the visual core description sheets.

X-ray CT images have multiple uses, from early assessment of cores to description and synthesis. For this reason, several hundred gigabytes of CT data were durably stored on a local database at the OsiriX interpretation station. All X-ray CT data will be available after the moratorium at the SIO7 Web site (sio7.jamstec.go.jp).

Lithology

Visual core descriptions

We followed conventional Ocean Drilling Program (ODP) and IODP procedures for recording sedimentologic information on visual core description (VCD) forms on a section-by-section basis (Mazzullo and Graham, 1988). Core descriptions were transferred to section-scale templates using shipboard database software J-CORES and then converted to core-scale depictions using Strater software. Texture (defined by the relative proportions of sand, silt, and clay) follows the classification of Shepard (1954). The classification scheme for siliciclastic lithologies follows Mazzullo et al. (1988).

The Graphic Lithology column on each VCD plots to scale all beds that are at least 2 cm thick. Graphic patterns do not show persistent interlayers <2 cm thick, but such intervals are identified as laminae in the Sedimentary Structures column. It is difficult to discriminate between the dominant lithologies of silty clay and clayey silt without quantitative grain size analysis, so we grouped this entire range of textures into the category “silty clay” on all illustrations. We did not use separate patterns for more heavily indurated examples of the same lithologies (e.g., silty clay versus silty claystone) because the dividing line is arbitrary. Figure F4 displays graphic patterns for all lithologies encountered during Expedition 315. Also shown are symbols for internal sedimentary structures, soft-sediment deformation structures, and severity of core disturbance in both soft sediment and indurated sedimentary rock.

Smear slides

Smear slides are useful for identifying and reporting basic sediment attributes (texture and composition), but the results are not quantitative. We estimated the abundances of biogenic, volcanoclastic, and siliciclastic constituents with the help of a visual comparison chart (Rothwell, 1989). Errors can be large, however, especially for fine silt and clay-size fractions, and reproducibility among different sedimentologists is poor. Smear slide analysis also tends to underestimate the amount of sand-size grains because they are difficult to incorporate evenly onto the slide. Thus, it would be misleading to report values as absolute percentages. Instead, our descriptive results are tabulated as visual percentage estimates, with values grouped into the following range categories:

- D = dominant (>50%).
- A = abundant (>20%–50%).
- C = common (>5%–20%).
- P = present (>1%–5%).

R = rare (0.1%–1%).

T = trace (<0.1%).

The relative abundance of major components was also validated by X-ray diffraction (see “**X-ray diffraction**”), and the absolute weight percent of carbonate was verified by coulometric analysis (see “**Organic geochemistry**”).

The sample location for each smear slide was entered into the J-CORES database with a sample code of SS using the Samples application. The position of each specimen is shown on the VCD slide editor column of the VCD application. We tabulated data in an Excel spreadsheet because data entry into J-CORES is prohibitively time-consuming and the program will not accept ranges of values for individual compositional categories.

X-ray diffraction

We completed routine XRD analyses of bulk powders using a PANalytical CubiX PRO (PW3800) diffractometer. Our principal goal was to estimate relative weight percentages of total clay minerals, quartz, plagioclase, and calcite using peak areas. Most of the samples were selected from intervals adjacent to whole-round samples, and most are part of sampling clusters with physical properties and carbonate. A few additional samples were collected periodically from such unusual lithologies as carbonate-cemented claystone and volcanic ash. Samples were freeze-dried, crushed with a ball mill, and mounted as random bulk powders. The instrument settings were as follows:

Generator = 45 kV and 40 mA.

Tube anode = Cu.

Wavelength = 1.54060 Å ($K_{\alpha 1}$) and 1.54443 Å ($K_{\alpha 2}$).

Step spacing = $0.005^{\circ}2\theta$.

Scan step time = 0.648 s.

Divergent slit = automatic.

Irradiated length = 10 mm.

Scanning range = $2^{\circ}2\theta$ to $60^{\circ}2\theta$.

Spinning = yes.

In order for our results to match those of ODP Leg 190 as closely as possible, the choice was made to use MacDiff version 4.2.5 software (www.ccp14.ac.uk/ccp/ccp14/ftp-mirror/krumm/Software/macintosh/macdiff/MacDiff.html) for data processing. Each peak's upper and lower limits were adjusted following the guidelines shown in Table T3. Calculations of relative mineral abundance utilized a matrix of normalization factors derived from integrated peak areas and singular value decomposition (SVD) (Table T4). As described by Fisher and Underwood (1995), calibration of SVD factors depends on the analysis of known weight-percent mixtures of min-

eral standards that are appropriate matches for natural sediments. SVD normalization factors were recalculated during Expedition 315 after the diffractometer's high-voltage power supply was replaced. Bulk powder mixtures for the Nankai Trough are the same as those reported by Underwood et al. (2003): quartz (Saint Peter sandstone), feldspar (Carich albite), calcite (Cyprus chalk), smectite (Camontmorillonite), illite (Clay Mineral Society IMT-2, 2M1 polytype), and chlorite (Clay Mineral Society CCa-2). Examples of diffractograms for standard mixtures are shown in Figure F5.

Average errors (SVD-derived estimates versus true weight percent) are total clay minerals = 3.5%, quartz = 2.1%, plagioclase = 0.8%, and calcite = 1.5%. In spite of its precision with standard mixtures, the SVD method is only semiquantitative and results for natural specimens should be interpreted with some caution. One of the fundamental problems with any bulk powder XRD method is the difference in peak response between poorly crystalline minerals at low diffraction angles (e.g., clay minerals) and highly crystalline minerals at higher diffraction angles (e.g., quartz and plagioclase). Contents of clay minerals are best characterized by measuring the peak area, whereas peak intensity may be easier and more accurate to quantify quartz, feldspar, and calcite. Analyzing oriented aggregates enhances basal reflections of the clay minerals, but this step is time consuming and requires isolation of the clay-size fraction to be effective. Errors also propagate as more minerals and peaks are added to the procedure. For clay mineral assemblages, the two options are to individually measure one peak for each mineral and add the estimates together (thereby propagating the error) or to measure a single composite peak at 19.4° to $20.4^{\circ}2\theta$. Another source of error is contamination of mineral standards by impurities such as quartz (e.g., the illite standard contains ~20% quartz). For trace quantities of a mineral and peaks with low intensity, use of negative SVD normalization factors may result in negative values of absolute weight percent. In such cases, we inserted the numerical value of 0.1% as a proxy for “trace.”

In the final assessment, calculated values of a mineral's weight percent should only be regarded as relative percentages within a four-component system of clay minerals + quartz + plagioclase + calcite. How close those estimates are to their absolute percentages within the mass of total solids will depend on the abundance of amorphous solids (e.g., biogenic opal and volcanic glass), as well as the total of all other minerals that occur in minor or trace quantities. For most natural samples, the absolute errors are probably between 5% and 10%. Thus, the primary

value of bulk powder XRD data should be to identify spatial and temporal trends in sediment composition and to assist with core-log integration.

Structural geology

One of the main objectives of Expedition 315 was to document the structural geology of the uppermost ~1000 m CSF at the site proposed for deep drilling (~2.5 km) during Stage 2 of the Nankai Trough Seismogenic Zone Experiment (NanTroSEIZE). The deep drilling program will cross a major thrust in the accretionary prism (referred to as the “megaspay,” as it merges at depth with the main décollement of the subducting plate boundary), and Site C0001 was planned to provide the first information on the composition and structural architecture of the hanging wall of this major thrust. Documentation of the structures at this site is also necessary to understand the deformation history and associated geochemical and physical processes related to the growth of the prism in this area. Deformational structures, therefore, may be critical to understanding the megaspay thrust and its role in seismogenesis along this margin.

With this in mind, we tried to document each structure observed in the split cores. In many cases, X-ray CT images of whole-round (i.e., unsplit) cores were used to identify structural features and better understand their 3-D geometry. Structural data, however, were only collected on split cores. Collected data were hand logged onto a printed form at the core table and then typed into both a spreadsheet and the J-CORES database. Where possible, structural data were also corrected for rotations related to drilling.

Observations and data collection

Core observations and measurements followed previous ODP procedures (e.g., ODP Legs 131, 170, and 190) by using a modified plastic protractor (Fig. F6) and included taking notes on a descriptive core log designed and printed during the first days of the expedition (Fig. F7; see 315_STRUCTURE in “[Supplementary material](#)”). During Expedition 315, however, we also had access to CT images of the cores for the first time ever in ocean drilling, and we collected essentially all of the data from the working half, rather than the archive half, of the split core. CT images were regularly used to aid in identifying structures and defining their 3-D form and distribution in the core. Using the working half of the split core provided greater flexibility in removing—and cutting, if necessary—pieces of the core for more careful study and measurement. Thin sections, X-ray fluorescence

samples, and XRD samples could also be tagged or collected as we described the core.

Orientations of planar and linear features in cored sediments were determined relative to the core axis, which represents vertical in the core reference frame, and the “double line” marked on the working half of the split core liner, which represents north (or 0° and 360°) in the core reference frame. To determine the orientation of a plane, two apparent dips of the planar feature were measured in the core reference frame and converted to a plane represented by either a strike and dip or a dip and dip direction. This conversion was accomplished using a spreadsheet, as described in “[Orientation data analysis based on the spreadsheet](#).” This approach had the advantage of increasing data processing efficiency and reducing errors in transferring and retyping data (e.g., by using both R. Allmendinger’s Stereonet program and a spreadsheet). One apparent dip was typically represented by the intersection of the planar feature with the split face of the core and was quantified by measuring the dip direction and angle in the core reference frame. Typical apparent dip measurements had a trend of 090° or 270° and ranged in plunge from 0° to 90°. The second apparent dip was usually represented by the intersection of the planar feature and a cut or fractured surface at a high angle to the split face of the core axis. In many cases this was a surface either parallel or perpendicular to the core axis. In the former cases, the apparent dip lineation would trend 000° or 180° and plunge from 0° to 90°; in the latter cases, the trend would range from 000° to 360° and plunge 0°. Linear features observed in the cores were always associated with planar structures (typically faults or shear zones), and their orientations were determined by measuring either the trend and plunge in the core reference frame or the rake (or pitch) on the associated plane. All data were recorded on the log sheet with appropriate depths and descriptive information.

A range of planar deformation structures was observed in Expedition 315 cores. Most can be classified as primarily belonging to one of three types of structures: faults, shear zones (or deformation bands), and “vein structures.” This is not meant to imply that all structures are only one type—in fact, many structures show features characteristic of all three types—but at this preliminary stage, and with limited thin section and other microscopic analyses, we chose to use a limited number of broad categories. Of course, descriptive modifiers and sketches provide additional information as to the similarities and differences of individual structures. Faults are relatively planar, narrow zones of deformation characterized by a single band of concentrated deforma-

tion at the scale of the core and CT image. Faults also typically show clear evidence of displacement, including offset markers (e.g., bedding, burrows, or small pumice fragments), fault drag, and slickensided rough or polished surfaces. Faults are bright in CT images, suggesting a higher density than that of the adjacent matrix. However, a systematic study of deformation structures and brightness (i.e., CT number) was not undertaken, so there may well be significant variations in brightness, and therefore density, within and between various structures. Shear zones (or deformation bands) are generally wider than faults and are typically composed of multiple sets or bands of concentrated deformation. In many cases, the outer edges of a shear zone are sharp and more planar than the anastomosing surfaces of deformation within the zone. CT images also suggest a range of densities within individual zones as well as between different shear zones. Vein structures include a variety of structures, many of which have been recognized during previous ocean drilling expeditions and have been interpreted as dewatering structures. This category of structures includes the classic sigmoidal-shaped suite of thin mud-filled veins first documented by Brothers et al. (1996), Cowan (1982), and Ogawa (1980), as well as other veinlike structures that appear darker than the surrounding sediment and brighter (or denser) in CT images. These other veinlike structures include single planar to subplanar features several millimeters thick but associated with only limited displacements and rare to poorly developed slickenlines. In some cases, veinlike structures extend subparallel to the core axis for decimeters; in other cases, they occur at moderate to low angles to the core axis and have limited extent. Apparent offsets in the split core include both normal and thrust displacements. Kink bands are another type of structure observed in cored sediments, but well-developed kink bands appear to be relatively rare. In fact, only two occurrences are documented, although more detailed analysis may show that some of the structures classified as faults or deformation bands evolved from kink or kinklike structures.

Slickenlines represent the only linear structures observed in the cored sediments and are often associated with steps or, less commonly, spoon-shaped indentations on the faulted or sheared surface, producing an asymmetry that reflects the sense of slip during deformation. For a review of sense of shear criteria associated with mesoscopic brittle deformation of rocks, see Petit (1987) and Angelier (1994). Steps were interpreted as extension cracks (or “R” shears activated as extension cracks) that connect en echelon “P” shears within the fault or shear zone. In some cases, the combined set of P shears

and extension cracks provides an indication of shear sense; in other cases, extension cracks or P shears alone were used as evidence for slip sense. Spoon-shaped indentations were interpreted as R shears with the fault or shear zone and indicated a sense-of-slip synthetic to the main fault or shear zone. Slickenlines and associated shear sense indicators therefore provided critical information regarding slip direction during deformation.

Paleomagnetic data were routinely used to correct drilling-induced rotations of cored sediments. Rotations were induced during RCB coring, as is common in ocean drilling, and unexpectedly with the HPCS. Rotations of the core liner used in the HPCS, including any retrieved sediments, were apparently induced as the cutting shoe was removed on the rig floor (see “[Paleomagnetism](#)”); the sense and magnitude of rotations observed in the sediments are at least consistent with this interpretation. The core liner may have also twisted and rotated as the cutting shoe was installed before coring, but this remains to be investigated. To correct for these rotations, we identified sections of cored sediment that were relatively coherent and continuous—that is, sections that were interpreted to have rotated as a single piece during drilling or core liner removal. These coherent sections were then matched with paleomagnetic data from the appropriate depth intervals and used to unrotate the planar and linear structures preserved in the core section. In cases where core sections were not continuous (generally this included core sections <10 cm in length), individual samples were placed in a core liner at 20 cm intervals, which is the sampling length of the long-core cryogenic magnetometer on the *Chikyu*.

Orientation data analysis based on the spreadsheet

A spreadsheet template was developed and used during Expedition 315 to calculate orientation data in both core and geographic reference frames from the linear data collected from the cores (e.g., Fig. [F8](#); see 315_STRUCTURE in “[Supplementary material](#)”). The core reference frame is defined such that the up-core direction is vertical upward, the core-splitting plane is east–west vertical, and the double-lined side of the working half points toward north (Fig. [F9](#)).

Calculation of plane orientation

For a bedding or fault plane, two apparent dips on two different surfaces (e.g., the split core surface, which is east–west vertical, and the horizontal or north–south vertical surface) were measured in the core reference frame as azimuths (measured clockwise from north, looking down) and plunges (Fig.

F10). A coordinate system was defined in such a way that the positive x -, y -, and z -directions coincide with north, east, and vertical downward, respectively (Fig. F9). If the azimuths and plunges of the two apparent dips are given as (α_1, β_1) and (α_2, β_2) , respectively, as in Figure F10, then the unit vectors representing these two lines, v_1 and v_2 , are

$$v_1 = \begin{pmatrix} l_1 \\ m_1 \\ n_1 \end{pmatrix} = \begin{pmatrix} \cos \alpha_1 \cos \beta_1 \\ \sin \alpha_1 \cos \beta_1 \\ \sin \beta_1 \end{pmatrix}$$

and

$$v_2 = \begin{pmatrix} l_2 \\ m_2 \\ n_2 \end{pmatrix} = \begin{pmatrix} \cos \alpha_2 \cos \beta_2 \\ \sin \alpha_2 \cos \beta_2 \\ \sin \beta_2 \end{pmatrix}.$$

The unit vector normal to this plane, v_n (Fig. F10), is then defined as follows:

$$v_n = \begin{pmatrix} l_n \\ m_n \\ n_n \end{pmatrix} = \frac{v_1 \times v_2}{|v_1 \times v_2|},$$

where

$$v_1 \times v_2 = \begin{pmatrix} m_1 & m_2 \\ n_1 & n_2 \\ l_1 & l_2 \\ l_1 & l_2 \\ m_1 & m_2 \end{pmatrix} = \begin{pmatrix} m_1 n_2 - m_2 n_1 \\ n_1 l_2 - n_2 l_1 \\ l_1 m_2 - l_2 m_1 \end{pmatrix}.$$

The azimuth, α_n , and plunge, β_n , of v_n are given by

$$\alpha_n = \tan^{-1}(m_n/l_n), \beta_n = \sin^{-1}n_n.$$

The dip direction, α_d , and dip angle, β , of this plane are α_n and $90^\circ + \beta_n$, respectively, when β_n is $<0^\circ$ (Fig. F11A). They are $\alpha_n \pm 180^\circ$ and $90^\circ - \beta_n$, respectively, when β_n is $\geq 0^\circ$ (Fig. F11B). The right-hand rule strike of this plane, α_s , is then given by $\alpha_d - 90^\circ$ (Fig. F11).

Calculation of slickenline rake

For a fault with slickenlines, the apparent rake angle of the slickenline, ϕ_a , was measured on the fault surface from either the 090° or 270° direction of the split-core surface trace (Fig. F12). Fault orientation was measured as described above. Provided that v_n and v_c are unit vectors normal to the fault and split core surfaces, respectively, the unit vector of this in-

tersection line, v , is perpendicular to both v_n and v_c (Fig. F12) and is therefore defined as follows:

$$v_i = \begin{pmatrix} l_i \\ m_i \\ n_i \end{pmatrix} = \frac{v_n \times v_c}{|v_n \times v_c|},$$

where

$$v_c = \begin{pmatrix} 1 \\ 0 \\ 0 \end{pmatrix}$$

and

$$v_n \times v_c = \begin{pmatrix} m_n & 0 \\ n_n & 0 \\ l_n & 1 \\ l_n & 1 \\ m_n & 0 \end{pmatrix} = \begin{pmatrix} 0 \\ n_n \\ -m_n \end{pmatrix}.$$

Knowing the right-hand rule strike of the fault plane, α_s (Figs. F11, F13), the unit vector, v_s , toward this direction is then

$$v_s = \begin{pmatrix} \cos \alpha_s \\ \sin \alpha_s \\ 0 \end{pmatrix}.$$

The rake angle of the intersection line, ϕ_i , measured from the strike direction is given by

$$\phi_i = \cos^{-1}(v_s \cdot v_i)$$

because

$$v_s \cdot v_i = |v_s||v_i| \cos \phi_i = \cos \phi_i, \therefore |v_s| = |v_i| = 1.$$

The rake angle of the slickenline, ϕ , from the strike direction is $\phi_i \pm \phi_a$, depending on the direction the apparent rake was measured from and the direction the fault plane dips toward. ϕ_a should be subtracted from ϕ_i when the fault plane dips west and ϕ_a was measured from either the upcore or 090° direction (Fig. F13A) or when the fault plane dips toward east and ϕ_a was measured from either the downcore or 090° direction (Fig. F13B). On the other hand, ϕ_a should be added to ϕ_i when the fault plane dips toward east and ϕ_a was measured from either the upcore or 270° direction (Fig. F13C) or when the fault plane dips west and ϕ_a was measured from either the downcore or 270° direction (Fig. F13D).

Azimuth correction using paleomagnetic data

Provided that a core is vertical, its magnetization is primary, and its bedding is horizontal, its paleomagnetic declination, α_p , indicates magnetic north when its inclination, β_p , is $\geq 0^\circ$ (Fig. F14A), whereas it indicates magnetic south when β_p is $< 0^\circ$ (Fig. F14B). The dip direction and strike of a plane in the geographic reference frame, α_d^* and α_s^* , are therefore

$$\alpha_d^* = \alpha_d - \alpha_p$$

and

$$\alpha_s^* = \alpha_s - \alpha_p$$

when

$$\beta_p \geq 0^\circ$$

and are

$$\alpha_d^* = 180^\circ + \alpha_d - \alpha_p$$

and

$$\alpha_s^* = 180^\circ + \alpha_s - \alpha_p$$

when

$$\beta_p < 0^\circ.$$

J-CORES structural database

Structural data entered in the J-CORES database VCD program include a visual (macroscopic and/or microscopic) description of core structures at a given section index and a record of planar structures in the core reference frame. Tablet PCs equipped with a wireless interface and writing recognition software were provided to allow data input directly from the core description tables. However, we found it more efficient to record the data on paper logs first (Fig. F15) and then transfer the data into the J-CORES database at a later time (see “J-CORES in practice for the structural geologist”). Data were also entered into a spreadsheet for postacquisition processing.

Data entry through the VCD program proceeds as follows:

1. Select expedition, site, hole, core, and section for which data will be read/written.
2. Select data to work with (e.g., CT image, structure description) and click **Hire** and **OK**.
3. Select a structure ID (e.g., bedding, fault) or create a new structure identifier (ID).
4. Select the section interval in which the structure is observed.

5. Fill the parameters related to this particular structure (comments and planar data; Fig. F15).

After saving, data are automatically uploaded to the *Chikyu* server and can be retrieved afterward as text or as an Excel file for processing. It is important to note that scientists are only allowed to write data in their own field of research and for their expedition (for example, an Expedition 315 structural geologist can only input structural data for Expedition 315). Any logged-in user has “read” access to the entire database.

J-CORES in practice for the structural geologist

Using the VCD program for real-time logging at the core table proved to be difficult for four main reasons. First, drawings are critical for structural description, yet they cannot be entered into the program via the tablet PC. Second, the handwriting recognition software is prone to errors. For example, the number 90 is commonly interpreted as the word “go,” which yields an error message in the number-only plane parameters box. This is particularly inconvenient because in a core reference frame the number 90 is used very often. Confusion also occurs between the numbers 1 and 7, which is somewhat more pernicious because it does not automatically yield an error message. Third, some numbers or combinations of numbers make the software systematically freeze, even if entered through a keyboard. Indeed, ~3% of our fault data could not be entered into J-CORES because of apparent bugs. When such bugs are encountered, the data saved in the last 10 min are usually lost because apparently their upload to the server is not instantaneous. Finally, the J-CORES VCD program is not well adapted for documenting multiple data that are linked or genetically related (e.g., fault planes, slickenlines, and sense-of-slip data; fold axes and axial planes; and bedding and current lineations). There are two options for working around this limitation while inputting fault data (Fig. F15). The first option is to use one structure ID (e.g., “normal fault”) and plane orientation and then enter the slickenline data in the comment box of the structure. In this case, the slickenline data are not exportable as an Excel spreadsheet. The second option is to enter two structure IDs (“normal fault” and “slickenline”) at the same depth interval. In this case both data may be exported, but as separate sets (i.e., the slickenline is not bound to the fault). In very deformed sections, it becomes almost impossible to know which slickenline belongs to which fault. In addition, the rake data of the slickenline must also be entered into the comment box because conversion of rake data into trend/plunge data is not supported by the program.

During Expedition 315, J-CORES proved to be a useful tool for data comparison and integration. We used the VCD program to develop a general overview of fault and shear zone densities throughout the cores. It was also used as a quick core photo display tool, convenient for the recognition of coherent intervals appropriate for paleomagnetic reconstruction work or for a quick recall of CT scan images.

How to improve future versions of J-CORES for structural geologists

Practical experience garnered during Expedition 315 reveals a number of positive and negative aspects of J-CORES. Specific recommendations for improvement are as follows:

- Enhance the handwriting recognition software,
- Provide a means to record sketches,
- Correct the bugs related to the entry of numerical data,
- Increase the frequency and/or speed of data uploads to offset data loss as a result of crashes,
- Allow fault data to include kinematic information (i.e., lineation orientation and sense) as a single set in any format (strike, dip; dip direction, dip; strike, dip, dip quadrant; or slickenline rake or trend),
- Allow direct copy and paste of the data to and from the J-CORES database (e.g., from the J-CORES database to Excel and vice versa), and
- Reduce the number of icons to click on for one action (e.g., skip **Apply** before **Save** when entering a new structure).

Biostratigraphy

Calcareous nannofossils

Calcareous nannofossil biostratigraphic classification of sedimentary sequences recovered during Expedition 315 follows the recent review by Raffi et al. (2006), who astrobiochronologically calibrated Pleistocene to late Oligocene calcareous nannofossil datum events. Astrochronological age estimates for the Neogene rely on the geologic timescale developed by the International Commission on Stratigraphy (ICS) in 2004 (Lourens et al., 2004). Included biohorizons are based on standard nannofossil zonations established by Martini (1971) and Okada and Bukry (1980) with zonal modifications by Young (1999). Size-defined species of the genera *Gephyrocapsa* and *Reticulofenestra* were placed into size categories as proposed by Young (1999) instead of referring to species names, which vary widely among different authors. Consequently, in the late Pleistocene the

abundance change between *Gephyrocapsa* spp. (>3.5 μm) and *Emiliana huxleyi* was used instead of the crossover between *Gephyrocapsa caribbeanica* and *E. huxleyi*.

Biostratigraphic event zonal markers for the Cenozoic are shown in Figure F16, along with events defining zonal boundaries and additional biohorizons. In Table T5, well-dated nannofossil datums used during Expedition 315 are listed.

Methods

For nannofossil analyses, the core catcher sections of each core were sampled. Samples from other sections were sometimes included when nannofossils were not abundant in core catcher material. Preparation of smear slides for light microscope examination followed standard procedures. Taxon identification was carried out under plane- and cross-polarized light using a Zeiss Axio Imager.A1m microscope at 1250 \times magnification. Abundance, preservation, and zonal data for each sample investigated were recorded in the J-CORES database. To determine species abundance, specimens in 10–20 fields of view were counted, depending on overall nannofossil abundance. Moreover, the slide was scanned along its entire long axis for additional taxa. The following scale was used to estimate the relative abundances of individual taxa present in each sample:

B = barren (none).

R = rare (<0.1%).

F = few (0.1% to <1%).

C = common (1% to <10%).

A = abundant (10%–50%).

D = dominant (>50%).

Assessments of calcareous nannofossil preservation were based on the following criteria:

P = poor, severe dissolution, fragmentation and/or overgrowth has occurred; primary features may have been destroyed, and many specimens can not be identified at the species level.

M = moderate, dissolution and/or overgrowth are evident; besides frequently broken nannofossils, the number of delicate forms is reduced.

G = good, little or no evidence of dissolution and/or overgrowth; diagnostic characteristics are preserved and nearly all species (~95%) can be identified.

VG = very good, no evidence of dissolution and/or overgrowth; diagnostic characteristics are preserved and all specimens can be identified.

Some of the additional samples from core sections were only scanned for biostratigraphic key species without recording the abundances of the entire assemblage. These samples were not included in the range charts (see the “[Expedition 314 Site C0001](#)” chapter) but may be listed in the table of nannofossil events (Table [T5](#)).

Planktonic foraminifers

The planktonic foraminifer zonation of Blow (1969) and astronomically calibrated biohorizons of Neogene planktonic foraminifers compiled by the ICS in 2004 (Lourens et al., 2004) were applied for this expedition. In addition, useful biohorizons were employed from literature in the field and converted in age to the current geomagnetic polarity timescale (GPTS).

The last occurrence (LO) of *Globigerinoides ruber rosa* was located at 0.12 Ma in the Indian and Pacific Oceans by Thompson et al. (1979) and confirmed by others (i.e., Li et al., 2005, at ODP Site 1143, South China Sea). The LOs of *Neogloboquadrina asanoi* and *Globoquadrina dehiscens* and the first occurrence (FO) of *Globoconella inflata* modern form were correlated with geomagnetic polarities at ODP Sites 1150 and 1151 off northeast Japan (Motoyama et al., 2004). The coiling direction change of *Pulleniatina* spp. from sinistral to dextral has been reported just above Chron C2n (Olduvai) in the Boso Peninsula of central Honshu, Japan (Oda, 1977). The FOs of *Truncorotalia crassaformis hessi*, *Truncorotalia tosaensis*, and *Pulleniatina primalis*; the first consistent occurrence of *Neogloboquadrina acostaensis*; and the LO of *Paragloborotalia mayeri* were compiled by Berggren et al. (1995) and converted in age to the current GPTS. These biozones and biohorizons are shown in Table [T6](#) and Figure [F16](#).

Methods

About 10 cm³ of sediment from core catcher sections was collected for foraminifer analyses. Soft sediment samples were disaggregated using hydrogen peroxide solution. Firm mudstone samples were treated by the sodium tetraphenylborate method (Hanken, 1979). After samples were macerated, each sample was wet-sieved through a screen (63 μm opening). Planktonic foraminiferal specimens >125 μm were taken from the dried residues. Semiquantitative estimates of species were made of the relative abundance as follows:

- + = present (<4% or species from samples yielding <100 total individuals).
- R = rare (4% to <8%).
- C = common (8% to 16%).
- A = abundant (>16%).

Preservation of each sample was recorded by the following criteria:

- P = poor, dissolution of surface structure and fragmentation are observed; most individuals cannot be identified at the species level.
- M = moderate, dissolution and fragmentation are commonly evident; some individuals are hard to identify.
- G = good, no dissolution; fragmentation of individuals has slightly occurred.

Abundance and preservation data for each sample investigated were uploaded into the J-CORES database.

Paleomagnetism

Laboratory instruments

The Paleomagnetism laboratory on board the *Chikyu* is located on the starboard side of the core processing deck. Most of the equipment is housed in a large (7.3 m × 2.8 m × 1.9 m) magnetically shielded room, with its long axis parallel to the ship transverse. The total magnetic field inside the room generally equals 1% of Earth’s magnetic field. The room is large enough to comfortably handle standard IODP core sections (~150 cm). The shielded room houses the equipment, instruments, and ancillary items described in this section.

Superconducting rock magnetometer

The 760-8.1 cm long-core superconducting rock magnetometer (2G Enterprises) unit is ~6 m long. A 1.5 m split core liner passes through a magnetometer, an alternating-field (AF) demagnetizer, and an anhysteretic remanent magnetizer. The system includes three sets of superconducting pickup coils, two for transverse movement measurement (x- and y-axes) and one for axial moment measurement (z-axis). These pickup coils have a large volume of uniform response to a small magnetic dipole. When a sample is inserted into the pickup coil region, persistent currents are generated in all three pickup coils. To prevent magnetic noise from being picked up from sources other than samples inserted into the system, both the pickup and coil structures and the direct-current superconducting quantum interference device (DC-SQUID) sensors have superconducting shields placed around them. The noise level of the magnetometer is <10⁻⁴ mA/m for a 10 cm³ volume sample. The superconducting rock magnetometer (SRM) dewar system has a capacity of 90 L of liquid helium. The magnetometer includes an automated sample handler system (2G804) consisting of aluminum and fiberglass channels designated

to support and guide long core movement. The core itself is positioned in a nonmagnetic fiberglass carriage that is pulled through the channels by a pull rope attached to a geared high-torque stepper motor. A 2G600 sample degaussing system is coupled to the SRM to allow automatic demagnetization of samples up to 300 mT with a standard air-cooled solenoid (model 2G601S) and up to 180 mT with a transverse split pair (model 2G601T). The system is completely controlled by an external computer. Because it is used with the automatic sample handler, a complete sequence of measure and degauss cycles can be completed without removing the long core from the holder.

A 2G615 anhysteretic remanent magnetization (ARM) system is included to enable magnetization of rock samples during demagnetization. Magnetization is achieved by applying a direct current (DC) magnetic field in the range of 0 to ± 4 Gauss during the degaussing process.

Spinner magnetometer

A spinner magnetometer, model SMD-88 (Natsuhara Giken Co., Ltd.) is also available for remanent magnetization measurement. The noise level is $\sim 5 \times 10^{-7}$ mAm². The measurable range is from 5×10^{-6} to 3×10^{-1} mAm². Five standard samples with different intensities are prepared to calibrate the magnetometer. Standard 2.5 cm diameter \times 2.1 cm long samples can be measured in three or six positions, the hole sequence taking ~ 1 and 2 min, respectively. Remanent intensity of Expedition 315 samples prevented the use of the spinner magnetometer.

Alternating-field demagnetizer

The alternating-field demagnetizer DEM-95 (Natsuhara Giken Co., Ltd.) is set for demagnetization of standard discrete samples of rock or sediment. The unit is equipped with a sample tumbling system to uniformly demagnetize up to an AF peak of 180 mT.

Anhysteretic remanent magnetization

The DTECH alternating-field demagnetizer D-2000 is available to impart ARM to discrete samples, in which a DC magnetic field is produced continuously across the AF demagnetizer coil. The user can select the demagnetization interval over which the field is applied (maximum AF = 200 mT, maximum DC field = 1.5 mT), producing partial anhysteretic remanent magnetization.

Thermal demagnetizer

The thermal demagnetizer TDS-1 (Natsuhara Giken Co., Ltd.) has a single chamber for thermal demagne-

tization of dry samples over a temperature range from room temperature to 800°C. The boat holds up to 8 or 10 cubic or cylindrical samples, depending on the exact size. The oven requires a closed system of cooling water, which is conveniently placed next to the shielded room. A fan next to the μ -metal cylinder that houses the heating system is used to cool samples to room temperature. The measured magnetic field inside the chamber is ≤ 10 nT.

Anisotropy of magnetic susceptibility system

The Kappabridge KLY 3, designed for anisotropy of magnetic susceptibility (AMS) measurement, is also available. Data are acquired from spinning measurements around three different axes. Deviatoric susceptibility tensor can then be computed. An additional measurement for bulk susceptibility completes the sequence. Sensitivity for AMS measurement is 2×10^{-8} (SI). Intensity and frequency of field applied are 300 A/m and 875 Hz, respectively. This system also includes the temperature control unit (CS-3) for temperature variation of low-field magnetic susceptibility of samples.

Pulse magnetizer

The pulse magnetizer MMPM10 (Magnetic Measurement Ltd.) can produce a high magnetic field. A maximum field of 9 T with a 7 ms pulse duration can be produced by the 1.25 cm diameter coil. The 3.8 cm coil generates a maximum field of 2.9 T. During Expedition 315, this apparatus was not operative.

Fluxgate magnetometer

The Walker portable three-axis fluxgate magnetometer (model FGM-5DTAA) measures small ambient fields with a range of ± 100 μ T and a sensitivity of 1 nT. The sensor fits into small spaces, such as the sample access tube of the cryogenic magnetometer. The magnetometer was also used to monitor the total field in the shielded room and as a thermal demagnetizer.

Hall-effect magnetometer

A Hall-effect magnetometer (model MG-5DP), capable of measuring DC and alternating current fields over three orders of magnitude (± 0.01 , ± 0.1 , and ± 1 T), is available for calibrating demagnetization coils and measuring strong DC fields.

Methods

Remanent magnetization was measured using the shipboard long-core cryogenic magnetometer. Continuous core measurements were typically made at 5 cm intervals with 20 cm long headers and trailers.

The response curve from the sensor coils of the cryogenic magnetometer was measured and corresponds to a region ~20 cm wide (Fig. F17); therefore, only measurements taken every 20 cm are independent from each other. Measurements at core and section ends, whole-round locations and voids, and within intervals of drilling-related core disturbance were not measured or were removed during data processing. The background noise of the instrument, as well as the liquid helium boil-off, seem to be amplified by the ship's movement compared to shore-based instruments, and the first background noise estimate was $\sim 10^{-10}$ Am². The relatively large volume of core material within the sensing region compensates for the relatively high background noise, and with very few exceptions sediment magnetization was well above instrumental noise level.

Sampling coordinates

The standard IODP core coordinate system was used, where +x is the vertical upward direction when the core (archive half) is on its curved side, +y is the direction to the left along the split-core surface when looking upcore, and +z is the downcore direction (Fig. F18). Coordination of the ship's long-core magnetometer is shown in Figure F18, along with standard IODP core coordination. The "flipping" function of the control software (Long Core version 3.4) enables 180° rotation of the x- and y-axes about the z-axis. By switching, working and archive halves can be measured in the same coordination. AF demagnetization on the archive halves was performed routinely with the inline AF demagnetizer at typical fields of up to 20 or 30 mT in order to avoid compromising future shore-based paleomagnetic studies. Occasionally we reached 80 mT, the maximum AF attainable field, on samples taken from working halves from intervals where a more precise direction was needed for structural correction purposes. Such a high AF value was required to overcome the drilling-induced overprint (see "[Paleomagnetism](#)" in the "Expedition 315 Site C0001" chapter).

Paleomagnetic core reorientation

Azimuthal orientation of drilled core material is of great importance when modeling directional properties of rock formations. Paleomagnetism can be used to determine the core azimuth by providing a reference direction from the drilled rocks. Paleomagnetic core reorientation has been used successfully for a number of years (e.g., Fuller, 1969; Kodama, 1984; Shibuya et al., 1991; Pares et al., 2007, in press). The procedure is based on determining the direction of stable remanent magnetization (either viscous rema-

nent magnetization or primary magnetization) with respect to a common reference line that is scribed the length of the core. Provided that the reference magnetic pole is known, the orientation of the paleomagnetic vector is then used to restore the core azimuth. The horizontal component of the mean characteristic remanent magnetization (ChRM) direction makes an angle with the reference line, which specifies the rotation of the core relative to the geographic coordinates.

To restore core orientation to geographic coordinates, the mean paleomagnetic direction is computed for samples sharing a common reference line. We have systematically used the archive half, which is marked at the bottom with a single reference line (the working half has a double line). After visual inspection of the AF demagnetization plots, we determined whether the blanket demagnetization at the highest peak (typically 20 mT) truly reflects the ChRM of the sediments. Measurements made on the uppermost and lowermost 20 cm have been typically disregarded to avoid end-core effects.

Our assumptions are as follows:

- The true paleomagnetic direction points to present-day geographic north. A given section has enough measurements to average secular variation.
- Bedding is horizontal or subhorizontal.
- Core is vertical.
- Sedimentary unit is in situ and has not experienced any vertical axis rotation.

Physical properties of the cored sediment, including voids, drilling disturbance, and flow-in, have determined to large extent the applicability of the paleomagnetic method for core reorientation. Hence, our "mean directions" are based on the statistical analysis of individual sections (from ~30 to 150 cm long) only when there is no visual evidence for general core disturbance or twisting. Even so, we noticed seemingly undeformed core sections that showed evidence of severe core twisting (Fig. F19). We think that the origin of such core twisting, when using the HPCS, is related to the extraction of the liner from the barrel when the core is on board. In order to extract the liner, operators have to first remove the shoe, which requires twisting counterclockwise.

For intervals of particular interest for structural geology (see "[Structural geology](#)") we have taken two different approaches for core reorientation:

1. Discrete samples: small cubic (8 cm³) samples were cut from the working half in order to determine paleomagnetic direction. We used the "discrete sample" option of the SRM magnetom-

eter. This allows automatically measuring up to six samples, 20 cm apart.

2. Biscuits: for homogeneous segments containing structures that had to be reoriented (see “**Structural geology**”), we measured entire (up to ~15 cm) core segments. In this case, we measured the samples as “continuous samples” in the SRM, also 20 cm apart.

Magnetic reversal stratigraphy

Magnetic polarity was calculated using inclination-only data from continuous core measurements. Site C0001 has a latitude of 33°14.5', which translates into an expected inclination of ~52° for at least Neogene and Quaternary sediments. This inclination is high enough to base the polarity interpretation (normal or reversed) on the sign of the magnetic inclination (positive or negative).

Typical steps used to establish magnetic reversal stratigraphy included the following:

1. Visually inspect the demagnetization plots using the Long Core software.
2. Obtain remanent magnetization directions after 20 mT or the highest (blanket) demagnetization step and group them by sections.
3. Locate disturbed and “flow-in” intervals in core descriptions and discard those intervals from the data set; also, for RCB cored sediments, determine the position of “biscuits” in order to group the paleomagnetic data accordingly.
4. Exclude the top and bottom ~15 cm (response of the pick up coils is ~20 cm).
5. Check that there are at least four consecutive data points (= measuring intervals) with the same inclination sign to define a polarity chron.

Whenever possible, we offer an interpretation of the magnetic polarity, with the naming convention following that of correlative anomaly numbers prefaced by the letter C (Tauxe et al., 1984). Normal polarity subchrons are referred to by adding suffixes (e.g., n1, n2, etc.) that increase with age. For the younger part of the timescale (Pliocene–Pleistocene) we often use traditional names to refer to the various chrons and subchrons (e.g., Brunhes, Jaramillo, Olduvai, etc.). In general, polarity reversals occurring at core ends have been treated with extreme caution.

The ages of the polarity intervals used during Expedition 315 are a composite of four previous magnetic polarity timescales (Gradstein et al., 2004) (Table T7; Fig. F16).

Discrete samples

Discrete sampling (“routine sampling”) was completed for shore-based detailed studies. On average, about one standard sample (~8 cm³) was taken every 60 cm, but the actual spacing largely depends on the properties of the core material (e.g., flow-in, coring disturbances, etc.) and the preliminary paleomagnetic record obtained with the pass-through magnetometer. A few pilot specimens were demagnetized on board using both AF and thermal demagnetization. Results are shown in the corresponding summary.

Data reduction and software

Data visualization is possible because of the Long Core software that controls the SRM. However, that facility doesn't allow any computation of ChRM directions. The following programs have been used to interpret data (Tauxe, 1998):

- “plotmag” makes orthogonal and equal area projections of input demagnetization data.
- “boodi” calculates bootstrap statistics for a group of vectors.
- “plotdi” makes equal area plots of data, with uncertainties.
- “pca” calculates a best-fit line through specified data.
- “incfish” estimates the Fisher mean inclination and 95% confidence bounds from inclination-only data using the method of McFadden and Reid (1982).

Inorganic geochemistry

Interstitial water collection

Shipboard interstitial water samples were generally obtained from 20 to 45 cm long whole-round cores from the bottom of the third section of each core (labeled “Section 4”). Three whole-round cores were collected from the uppermost 10 m. These cores consisted of a clay matrix, and core recovery was adequate to produce at least five sections. Whole-round samples were sectioned and capped upon core recovery in the core cutting area and taken to the laboratory for immediate X-ray CT scanning. Provided no significant sedimentary or tectonic structures were observed in X-ray CT images, these samples were placed in a nitrogen-filled glove bag and flushed with nitrogen gas three times before squeezing. When there were too many samples to process immediately, samples were sealed in a small nitrogen-filled plastic bag and stored in a 4°C refrigerator until further processing.

The core liner was extracted from a whole-round core while it remained in a nitrogen-filled glove bag. The surface of each whole-round core was carefully scraped to avoid sediments that had potentially been contaminated from seawater, drilling fluid, oxidation, and smearing in the core liner. The clean inner parts of the core were then placed into a Manheim-type titanium squeezer (Manheim, 1966) and squeezed with a laboratory hydraulic press at gauge pressures up to 24,000 lb (with a piston diameter of 5 cm, this translates to a pressure of ~55 MPa). Interstitial water was passed through two rinsed filter papers fitted on two to four 300 mesh stainless steel screens at the bottom of the squeezer. Fluids from the squeezing process passed through a 0.45 μm disposable filter into an acid-washed (10% HCl) 50 mL plastic syringe. Interstitial water was subsampled for shipboard and shore-based analyses. All high-density polyethylene (HDPE) sample vials intended for minor and trace element analysis were cleaned by immersion in 55°C 10% trace metal grade 12N HCl for a minimum of 24 h and were subsequently rinsed with Millipore 18.2 M Ω -cm Type 1 ultrapure (Milli-Q) water and dried in a class 100 laminar flow clean hood.

All samples designated for shipboard minor and trace element analysis were acidified with subboiled 6N HCl at a ratio of 4 mL of subboiled 6N HCl per liter of sample at least 24 h prior to inductively coupled plasma-atomic emission spectroscopy (ICP-AES) or inductively coupled plasma-mass spectrometry (ICP-MS) analysis to dissolve any metallic oxide precipitates that may have formed after squeezing. Subsamples were collected for shore-based isotopic (O, H, Sr, Cl, Li, B, I, and S), rare earth elements (REE), Cd, Y, transition metals, and U series analyses. These subsamples were stored in detergent or acid-washed HDPE bottles (REE, Cd, and Y samples were acidified with subboiled 6N HCl at a ratio of 4 mL of subboiled 6N HCl per liter of sample within a few days of sampling). Additional subsamples were distributed for analyses of dissolved organic/inorganic carbon in crimp-cap glass vials with HgCl₂ and HOSO₂NH₂ and analyses of volatile fatty acids in pre-combusted glass vials that were transferred to a freezer held at -20°C.

Interstitial water analysis

Interstitial water samples were routinely analyzed for salinity as total dissolved solutes with an RX-5000 α refractometer (Atago) and for pH and alkalinity by Gran titration with a Metrohm autotitrator soon after interstitial water was extracted. The volume of titrant used for each analysis was recorded for future reference. Chloride concentration was measured on

a 100 μL subsample by titration using silver nitrate (AgNO₃) in a 0.2M sodium nitrate (NaNO₃) solution. International Association for the Physical Sciences of the Ocean (IAPSO) standard seawater was used as a quality control measure by repeated analysis until the relative standard deviation was a maximum of 0.8%.

Sulfate and bromide concentrations were measured by ICS-1500 ion chromatography (Dionex) using subsamples that were diluted 1:100 (10 μL in 990 μL) with Milli-Q water. This dilution provided quality peak detection for chloride, bromide, and sulfate. Chloride data were used only to check the quality of the dilution step. IAPSO standard seawater aliquots (2.5, 5, 7.5, and 10 μL in a total of 1000 μL) were analyzed at the beginning and end of each run as a quality control measure and to monitor potential drift in sensitivity throughout a particular run.

Dissolved phosphate concentration was measured using a colorimetric method with the aid of an UV-2550PC spectrophotometer (Shimadzu) at an absorbance of 885 nm. Because the concentration of phosphate in the analysis solution must be <10 μM , an appropriate aliquot of sample or standard solution (100 or 600 μL) was diluted to 1.1 mL with Milli-Q water (1000 or 500 μL) in a plastic tube. The 2 mL mixed solution (ammonium molybdate, sulfuric acid, ascorbic acid, and potassium antimonyl tartrate) was added to the tube and was well mixed; the tube was capped and kept at room temperature to develop color. A calibration curve was provided from a series of phosphate standard solutions (KH₂PO₄) of 25, 50, 50, 75, 100, 200, and 250 μM with a reproducibility better than 0.3%.

Dissolved ammonium concentration was also determined with the UV-2550PC spectrophotometer at an absorbance of 640 nm. Either 0.1 or 0.05 mL of sample aliquot was diluted with 1 or 2 mL Milli-Q water, 0.5 mL phenol ethanol, 0.5 mL sodium nitroprusside, and 1 mL oxidation solution (sodium hypochlorite and alkaline citrate) in a capped plastic tube and was kept in the dark at room temperature for >3 h to develop color. A calibration curve was provided from a series of ammonium standard solutions (NH₄Cl) of 0.5, 1.0, 2.0, 5.0, and 10 mM with a reproducibility better than 0.3%.

Concentrations of sodium, magnesium, calcium, potassium, strontium, lithium, iron, manganese, barium, silicon, and boron were obtained by ICP-AES using an Ultima2 (Horiba Jobin Yvon) designed with a radial viewing plasma orientation and two Czerny Turner monochrometers for parallel analysis of sample elements and internal standards. The major ions (Na, Mg, Ca, and K) were diluted by a factor of 501

by addition of a 30 μL sample to 15 mL of 0.15N nitric acid spiked with Y (10 ppm Y in a 1% ultrapure double-distilled nitric acid solution). Standardization of the major ions was achieved by successive dilution of IAPSO standard seawater to 100%, 75%, 50%, and 25% relative to the 1:501 primary dilution ratio. Because of the extremely high dilution ratio, no attempts were made to adjust for variable matrix effects. In the case of high (>1 mM) concentrations of Sr and Li in samples, additional dilutions of IAPSO standard seawater were prepared and spiked with a range of Li and Sr primary standards to measure these elements along with the major cations. The minor ions (Sr, Li, Fe, Mn, Ba, Si, and B) were diluted by a factor of 20 (0.5 mL sample with 9.5 mL of the same 10 ppm Y solution described above). Because of the high concentration of matrix salts in the pore water samples at a 1:20 dilution, matrix matching of the calibration standards was necessary. The matrix solution that approximated IAPSO standard seawater major ion concentrations was prepared from the following salts in 1 L of Milli-Q water acidified with 4 mL of ultrapure double-distilled 6N HCl: 27 g NaCl, 3.8 g MgCl, 1.0 g CaCO₃, and 0.75 g KCl. No sulfate was added to the matrix because the pore water sulfate concentrations decreased rapidly in the first few cores. There was some concern that the salts used for the matrix were not trace metal grade, but analysis of the matrix solution revealed that the concentrations of minor elements in the matrix were less than or equal to the lowest standards analyzed and did not significantly affect the signal-to-noise ratio of the measurements. Because the matrix solution was not a true blank, the procedural blank used was a dilution of 1% ultrapure nitric acid in the Y solution and only the slope of the calibration curve was used for quantification. A stock standard solution was prepared from ultrapure primary standards (SPC Science PlasmaCAL) in 1% ultrapure 15N nitric acid. The relative concentrations of elements in the stock standard were adjusted based on results from Legs 131 and 190 because these samples were taken from sediments from similar geological conditions. The stock solution was then diluted in the same 1% nitric acid solution to concentrations of 50%, 25%, 10%, 5%, and 1%. A 1.25 mL aliquot of each stock solution was added to 8.75 mL of matrix to produce a series of standards that could be diluted using the same method as the samples for consistency. A copious supply of stock and matrix solutions was prepared during this expedition for use on the next expedition so that the analytical results of the two expeditions will be comparable. The final matrix-matched 100% standard solution contained the following concentrations of elements: 3000 μM B, 400 μM Li, 1000 μM Si, 50 μM Mn, 50 μM Fe, 400 μM Sr, and

200 μM Ba. Because values of many of these elements in IAPSO standard seawater are either below detection limits (e.g., Fe and Mn) or variable, a 10% matrix matched standard was repeatedly analyzed to calculate the precision of the method.

Several trace elements (V, Mn, Fe, Cu, Zn, Mo, Rb, Cs, Pb, and U) were analyzed using an Agilent 7500ce ICP-MS equipped with an octopole reaction system to reduce polyatomic and double-charge interferences. To calibrate for interferences by the major ions Na, Cl, K, Ca, and S on some of the transition metals (ClO and SOH on V, Na and CaOH on Cu, and S on Zn), solutions were prepared containing these elements at concentrations similar to IAPSO standard seawater values. These solutions were analyzed at the beginning of each run and an interference correlation was applied based on the average counts per second (cps) measured on the standard solutions divided by the abundance of the interfering elements. This ratio was multiplied by the known concentration of the major ions in the samples based on previous analysis, and the result was subtracted from the measured cps of the sample. Before diluting the samples, a 100 μL aliquot of 500 ppb in standard was added to the empty analysis vials. Samples were then diluted into these vials to 3% in 1% HNO₃ (150 μL sample with 4.85 mL 1% HNO₃) based on previous determination of the detection limits and low concentrations of the elements of interest. A primary standard solution was made that matched the maximum range of predicted concentrations based on published results of deep-sea pore fluid compositions in a variety of settings. The composition of the standard is as follows: 20 ppb V; 40 ppb Cu, Mo, Pb, and U; 140 ppb Zn; 500 ppb Rb; and 5 ppb Cs. This primary standard was diluted in 1% ultrapure 15N nitric acid to relative concentrations of 50%, 25%, 10%, 5%, and 1%. These standards were then diluted to 3%, similar to the samples, with the addition of 150 μL of a 560 mM NaCl solution and 4.7 mL of 1% HNO₃ to account for matrix suppression of the plasma ionization efficiency. The 25% standard was diluted this way and analyzed every eight samples throughout every analysis series for precision and in order to correlate results from different analysis dates. Blanks were also analyzed every eight samples, and the detection limits were determined as three times the standard deviation of a procedural blank of Milli-Q water acidified with 4 mL of subboiled 6N HCl per liter. No standard reference material was available on the ship to verify the accuracy of the analysis. Accuracy was determined by analyzing 31 (40%) of the interstitial water samples collected during the expedition using a high-resolution ICP-MS (Finnigan Element 2) at

Moss Landing Marine Laboratories (Hulme et al., 2008). Generally, ship- and shore-based analyses agreed for Cu, Mo, Pb, and U. Minor adjustments to the shipboard Rb (10%) and Cs (20%) were necessary. Shipboard V and Zn data were different from shore-based data and standard reference material by a factor of two, possibly indicating an issue with shipboard standards. Shore-based analysis also provides a measure of Y concentration. Shore-based data are shown in tables and figures for both sites (see the “Expedition 315 Site C0001” and “Expedition 315 Site C0002” chapters).

Oxygen and hydrogen isotopes

Interstitial water was also measured for its stable isotopic compositions of oxygen ($\delta^{18}\text{O}$) and hydrogen (δD) as primary shore-based analyses after the expedition. $\delta^{18}\text{O}$ and δD values were determined with the mass spectrometer, Delta Plus XP with Gas Bench II (Thermo Finnigan), at New Energy Resources Research Center, Kitami Institute of Technology, Japan. Results were calculated in permil delta notation against the Vienna standard mean ocean water (V-SMOW) with analytical precisions better than 0.1‰ for $\delta^{18}\text{O}$ and better than 1‰ for δD .

GRIND method

A method of pore water extraction for sediments with porosities <40% was used during Expedition 315. This method was initially developed by Cranston (1991) and later used by Wheat et al. (1994) to assess pore fluid composition under conditions where it was impossible to extract a sufficient supply for chemical analysis. During whole-round sampling of the uppermost 200 to 400 m CSF, a series of subsamples of ~5 to 10 cm of sediments were taken from samples when there was excess material after pore fluid extraction. These were taken to compare the GRIND results to traditional pore water extraction methods. Samples were initially scraped clean of the outer portions within the glove bag, wrapped in plastic wrap, and sealed in nitrogen-filled plastic bags. These were stored at 4°C for a period of 3 to 5 days.

Following the Cranston (1991) method, Milli-Q water was bubbled with nitrogen gas for a period of 48 h to remove dissolved oxygen. This water was then spiked with 10 ppm In standard to a final concentration of 100 ppb. This concentration was chosen in order to reach a diluted concentration of 1 ppb for ICP-MS analysis at 1% dilution. The purpose of the In standard was to calculate the degree of mixing between the interstitial waters and the distilled water that is added as part of the method. Sealed samples were placed in a nitrogen-filled glove bag along with

ball mill cylinders and the In solution. The samples were unsealed, broken into small pieces, and placed in the ball mill cylinders with three ceramic milling balls. Depending on the dryness of the samples and the volume of sample in the cylinders, between 1.5 and 3 mL of In solution was added prior to milling. A 3 mL subsample of the In solution was taken after each set of mills were filled. The milling cylinders were covered within the glove bag and taken immediately to the mill for grinding. The mill was operated at 400 rotations per minute (rpm) for a period of 5 min, and afterward the containers were placed back into the glove bag. The milling cylinders were opened in the glove bag and the ground samples were squeezed using the same methods described above. The volume of In solution added to the sample, the volume recovered after squeezing, the time of sample processing, and the corresponding In solution subsample were recorded for each sample.

Infrared thermal observation

Because the dissociation of gas hydrates is an endothermic reaction, observation of low-temperature anomalies on the surface of the core liner provides a means to identify sections that contain or contained gas hydrate. Therefore, infrared thermal observation of the surface of the core liner was used during ODP Legs 201 and 204 and IODP Expedition 311 to identify the distribution of gas hydrates immediately before core disturbance because of their dissociation.

During Expedition 315, a handheld infrared camera, the ThermaCAM SC640 (FLIR Systems), was used to visualize temperature distributions of the surface of several core liners before cores were sectioned in the core cutting area. The initial purpose of thermal imaging is to rapidly identify gas hydrate-bearing sections for immediate sampling and for stabilizing and storing the gas hydrate in liquid nitrogen for future shore-based analyses. Infrared images were acquired from the cores between 0 and 450 m CSF, which are within the gas hydrate stability zone.

Organic geochemistry

Shipboard organic geochemical analyses included volatile hydrocarbon contents ($\text{C}_1\text{--}\text{C}_4$); inorganic carbon and carbonate contents; and elemental analyses of total carbon, nitrogen, and sulfur. Procedures used during Expedition 315 follow Pimmel and Claypool (2001).

Gas analysis

A 5 cm³ sediment sample was collected with a cut-off plastic syringe, usually from the exposed end of Sec-

tion 1, and was extruded into a 20 mL glass vial. The vial was placed in an oven at 70°C for 30 min. The evolved gases were analyzed using an Agilent 6890N gas chromatograph (GC) equipped with a flame ionization detector (FID). This system determined the concentration of C₁–C₄ hydrocarbons with an FID. Chromatographic response on the GC was calibrated against five different authentic standards with variable quantities of low molecular weight hydrocarbons. When heavier molecular weight hydrocarbons (C₃ and higher) were detected, gas samples were analyzed on the natural gas analyzer (NGA). The NGA system consists of an Agilent 6890N GC equipped with four different columns, two detectors, both an FID and a thermal conductivity detector (TCD), and WASSON-ECE instrumentation. The NGA was used to measure C₁–C₁₃ hydrocarbons and nonhydrocarbons (CO, CO₂, O₂, and N₂). Compositions of gases in sediments were analyzed in at least one horizon per core.

Inorganic carbon

Inorganic carbon concentrations were determined using a Coulometrics 5012 CO₂ coulometer. About 10–12 mg of freeze-dried ground sediment was weighed and reacted with 2M HCl. The liberated CO₂ was titrated, and the change in light transmittance was monitored with a photodetection cell. The weight percentage of calcium carbonate was calculated from the inorganic carbon content, assuming that all evolved CO₂ was derived from dissolution of calcium carbonate, by the following equation based on molecular weight ratio:

$$\text{CaCO}_3 \text{ (wt\%)} = 8.33 \times \text{IC (wt\%)},$$

where IC = inorganic carbon. All carbonate minerals were treated as CaCO₃. Standard deviation for the samples is less than ±0.12 wt%.

Elemental analysis

Total carbon, nitrogen, and sulfur concentrations were determined using a Thermo Finnigan Flash EA 1112 CHNS analyzer with calibration using the synthetic standard sulfanilamide, which contains C (41.81 wt%), N (16.27 wt%), and S (18.62 wt%). About 10–20 mg freeze-dried ground sediment was weighed and placed in a tin container for carbon and nitrogen analyses. For sulfur analysis, the same amount of freeze-dried sediment was weighed and put in a tin container with the same amount of V₂O₅. Sediment samples were combusted at 1000°C in a stream of oxygen. Nitrogen oxides were reduced to N₂, and the mixture of CO₂, N₂, and SO₂ was sepa-

rated by GC and detected by TCD. Total organic carbon content was calculated by subtraction of inorganic carbon from total carbon. Standard deviation of carbon, nitrogen, and sulfur for the samples is less than ±0.1%. Accuracy for carbon and sulfur analysis was confirmed using two Geological Society of Japan reference samples. Analytical accuracy for JMS-1 (C = 1.69 wt% and S = 1.32 wt%) is 1.66 ± 0.2 wt% (N = 12) for carbon and 1.28 ± 0.06 wt% (N = 11) for sulfur. Analytical accuracy for JMS-2 (C = 0.39 wt% and S = 0.29 wt%) is 0.34 ± 0.02 wt% (N = 9) for carbon and 0.29 ± 0.04 wt% (N = 7) for sulfur. This accuracy includes weighing errors.

Microbiology

Core handling and sampling

Whole-round cores

Microorganisms in deep-sea sediments are expected to be sensitive to chemical and physical changes, particularly changes in oxygen, temperature, and pressure. Therefore, the core sections designated for microbiological sampling were transferred as quickly as possible from the rig floor to a refrigerator and were kept as whole sections until processed. However, because of the danger of explosion of core liners because of expanding sediment, some cores had to be kept on the rig floor for up to 3 h before X-ray CT scanning. Whole-round cores for microbiological analysis were cut based on X-ray CT scans. Our aim was to minimize potential contamination by selecting sections with minimal disturbance, such as voids or cracks. Three types of whole-round cores (10–20 cm) were taken for microbiological analysis. The first type was subsampled on board for cell counting, cultivation assays, and deoxyribonucleic acid (DNA) and ribonucleic acid (RNA) isolation. The second type was taken for cultivation studies. These cores were brought quickly to an anaerobic glove box (Coy Laboratory Products, Inc.), placed into an anaerobic pouch (Mitsubishi Gas Chemical Co., Inc.) with AnaeroPack (Mitsubishi Gas Chemical Co., Inc.), sealed with a plastic clip, and stored at 4°C for shore-based studies. The third type was subsampled for cell counting and then immediately placed into a plastic bag and stored at –80°C for onshore DNA-, RNA-, and intact polar lipids-based molecular analyses.

Subsampling of soft and hard sediments

Subsampling of soft-sediment whole-round cores was conducted with autoclaved tip-cut 5 mL syringes after scraping off the sediment surface with an ethanol-wiped spatula. Subsampling was restricted to sediments at or near the center of the cores because core

liners are not sterile and outer core surfaces are contaminated during drilling (Smith et al., 2000). For subsampling of semiconsolidated sediment, intact rock pieces were selected. The surface was washed with ethanol and/or scraped off with an ethanol-wiped spatula, and the rock was crushed with a hammer in an aluminum bag or ethanol-wiped aluminum folio.

Subsample treatment

Subsamples taken for DNA and RNA isolation were immediately frozen at -80°C . Subsamples taken for cell counting were fixed with 2% paraformaldehyde in phosphate-buffered saline (PBS; Invitrogen, pH adjusted to 7.6) overnight, washed two times with PBS, and finally stored in PBS:ethanol (1:1) at -20°C . Subsamples taken for cultivation assays were immediately placed into anaerobic serum bottles containing 35 g/L of Sigma sea salts (pH adjusted to 7.2) under counterflow of sterile-filtered (pore size = 0.22 μm) nitrogen. The slurries were homogenized by repeated shaking and vortexing and were stored at 4°C . Subsamples of the slurries were used for cultivating heterotrophic sulfate-reducing bacteria in a modified DSMZ medium 1040 (Table T8). Acetate, lactate, pyruvate, and ethanol (10 mM) were used as organic carbon and electron sources. Liquid cultures were incubated at different temperatures (9° , 37° , 50° , and 70°C) until the end of the expedition. Incubation will be continued on shore.

Drilling mud sampling

As it was not possible to do perfluorocarbon tracer contamination tests on board, preused drilling muds (seawater gel and kill mud) were used as control samples for microbiological analysis. Seawater gel (pH = 12.3) is a seawater-based bentonite mud used for drilling and coring throughout entire sections. It contains 0.5 m^3 seawater, 0.5 m^3 drill water, 60.0 kg bentonite, 2.0 kg caustic soda, and 2.0 kg lime. Kill mud is a freshwater-based, barite-weighted mud used to suspend or abandon the hole. It was not used before or during coring in this expedition. Kill mud (pH 11.3) contains 1 m^3 drill water, 60.0 kg bentonite, 1.0 kg caustic soda, 2.0 kg XCD-polymer, and 40.0 kg barite. The density of both drilling muds is 1.05 g/cm^3 . Mud samples were taken into autoclaved glass bottles and subsampled for cell counting, culturing, and molecular analysis. Subsamples for cell counting were fixed as described above. Subsamples for culturing and molecular analysis were stored at 4°C and -80°C , respectively.

Cell detection by fluorescence microscopy

Selected samples of fixed cells were stained on board with double-stranded DNA-binding SYBR Green I

stain for detecting cells (Lunau et al., 2005). Before staining, the fixed sediment slurry was vortexed and diluted in PBS:methanol (9:1). The mixture was sonicated at 50 W for 1 min with an ultrasonic homogenizer UH-50 (SMT Co., Ltd), and sediment particles were removed by centrifuging at 100 g for 2 min. An aliquot of the supernatant was mixed with 5 mL PBS and filtered through a black 0.2 μm pore-sized polycarbonate filter. The filter was washed twice with PBS and placed on an object glass. A coverslip was mounted on the filter with 8 μL of SYBR Green I staining solution. Cells were viewed with an epifluorescence microscope (ZEISS Axioplan 2 imaging microscope), and images were taken with a ZEISS AxioCam HRc camera and AxioVision AC software.

Physical properties

Continuous physical property measurements provide basic information to assist characterization of lithologic units and states of consolidation and deformation, as well as correlation of cored materials with downhole logging data. First, X-ray CT images were captured for all core sections. Then, gamma ray attenuation (GRA) density, magnetic susceptibility, natural gamma radiation, *P*-wave velocity, and electrical resistivity were measured using an MSCL system (Geotek Ltd., London, UK) for whole-round core sections (MSCL-W) after thermal equilibration at room temperature, $\sim 20^{\circ}\text{C}$. After MSCL-W measurements, thermal conductivity measurements were carried out on whole-round core sections for soft sediments and on split working-half cores for hard sediments and rocks. Digital photo image scanning and color spectrophotometry were carried out on the split surfaces of archive-half cores using the photo image capture logger (MSCL-I) and the color spectrophotometer (MSCL-C), respectively. MAD were measured on discrete subsamples collected from working-half core samples, as well as from clusters next to whole-round samples. Sediment shear strength was measured on working halves using vane shear and a penetrometer. *P*-wave velocity and electrical conductivity were measured in three orthogonal directions in 20 mm cubic samples. Details about each measurement are given below.

MSCL-W

Gamma ray attenuation density

A thin gamma ray beam was produced by a ^{137}Cs gamma ray source at a radiation level of 370 MBq within a lead shield with a 5 mm collimator. The gamma ray detector comprised a scintillator and an integral photomultiplier tube. Calculation of bulk

density from gamma ray attenuation was by the following equation:

$$\rho = 1/(\mu \times d) \times \ln(I_0/I),$$

where

- ρ = sediment bulk density,
- μ = Compton attenuation coefficient,
- d = sample thickness,
- I_0 = gamma source intensity, and
- I = measured intensity through the sample.

Because μ and I_0 are treated as constants, ρ can be calculated from I . We used a set of aligned aluminum cylinders of various thicknesses, surrounded by distilled water in a sealed core liner used for drilling, for calibration. Gamma counts were taken through each cylinder for long count time (60 s), and $\ln(I)$ was plotted against $\rho \times d$. Here ρ of each aluminum cylinder was 2.7 g/cm³, and d was 1, 2, 3, 4, 5, or 6 cm. The relationship between I and $\rho \times d$ can be expressed as follows:

$$\ln(I) = A (\rho \times d)^2 + B (\rho \times d) + C,$$

where A , B , and C are coefficients determined during calibration. These coefficients varied slightly during the expedition. The MSCL provided the values of I and d , and ρ was calculated with the equation above.

This density measurement was conducted every 4 cm for 4 s. The spatial resolution was 5 mm, so each data point reflects the properties of the closest 5 mm interval.

Porosity (ϕ) is calculated from MSCL density assuming a solid grain density (ρ_s) of 2.7 g/cm³ and a pore fluid density (ρ_f) of 1.024 g/cm³:

$$\phi = (\rho_s - \rho)/(\rho_s - \rho_f).$$

Magnetic susceptibility

Magnetic susceptibility is the degree to which a material can be magnetized by an external magnetic field. A loop sensor (MS2C; Bartington Instruments Ltd.) with an 8 cm loop diameter was used for magnetic susceptibility measurements. An oscillator circuit in the sensor produces a low-intensity (8.0×10^{-4} mA/m RMS) nonsaturating, alternating magnetic field (0.565 kHz). Any material near the sensor that has a magnetic susceptibility causes a change in the oscillator frequency. This pulse frequency is then converted into magnetic susceptibility values. The spatial resolution of the loop sensor is ~4 cm and accuracy is 5%.

Like GRA density data, magnetic susceptibility data were obtained at 4 cm intervals with a 41 s acquisition time.

Natural gamma radiation

Natural gamma ray (NGR) emissions were recorded from all core sections to determine variations in the radioactive counts of the samples and for correlation with downhole NGR measurements. A lead-shielded counter, optically coupled to a photomultiplier tube and connected to a bias base that supplied high-voltage power and a signal preamplifier, was used. Two horizontal and two vertical sensors were mounted in a lead cube-shaped housing. Most X-ray emissions from rocks and sediment were produced by the decay of ⁴⁰K, ²³²Th, and ²³⁸U, three long-period isotopes. Spatial resolution was 120–170 mm, and NGR was measured every 15 cm for a 30 s period. Background radiation noise was 38 cps, measured by inserting a blank filled with distilled water.

P-wave velocity

The basic relationship for sonic velocity is

$$v = d/t,$$

where

- d = distance traveled through the core and
- t = traveltime through the core.

P-wave velocity transducers are mounted on the MSCL system and measure d and t horizontally throughout the whole core. Total traveltime measured between the transducers includes three types of “delay” as

- t_{delay} = delay related to transducer faces and electronic circuitry,
- t_{pulse} = delay related to the peak detection procedure, and
- t_{liner} = transit time through the core liner.

The effects of delays are calibrated using a core liner filled with pure water. For routine measurements on whole-round cores in core liners,

$$v_{\text{core}} = (d'_{\text{core}} - 2d_{\text{liner}})/(t_0 - t_{\text{pulse}} - t_{\text{delay}} - 2t_{\text{liner}}) \times 1000,$$

where

- v_{core} = corrected velocity through core (km/s),
- d'_{core} = measured diameter of core and liner (mm),
- d_{liner} = liner wall thickness (mm), and
- t_0 = measured total travel time (μ s).

Electrical resistivity

The noncontact resistivity sensor on the MSCL system operates by inducing a high-frequency magnetic field in the core from a transmitter coil, which in turn induces electrical currents in the core which are inversely proportional to the resistivity. Very small magnetic fields regenerated by the electrical current are measured by a receiver coil. To measure these very small magnetic fields accurately, a different technique has been developed that compares readings generated from the measuring coils to readings from an identical set of coils operating in air. Electrical resistivity data were obtained at 4 cm intervals.

Thermal conductivity

Thermal conductivity measurements were conducted on whole-round core samples from relatively shallow depths (<230 m CSF) and on split halves of cores from depths >230 m CSF.

A full-space single-needle probe TeKa TK04 unit (Blum, 1997) was utilized to measure thermal conductivity of unconsolidated sediments at three per core interval under conditions of full recovery. A small hole was drilled in the core liner, usually 26 cm from the top of each section. A 2 mm diameter temperature probe was inserted into the working half of the core section. At the beginning of each measurement, temperature in the samples was monitored automatically without applying a heater current until the background thermal drift was determined to be <0.2 mK/h. The heater circuit was then closed, and the temperature increase in the probe was recorded. During each 24 h period, three standard blocks with thermal conductivities of 0.517, 1.237, and 1.623 W/(m·K), respectively, were probed. Measurement results were then plotted against true values, and the slope of the linear regression was obtained. This slope was used to calibrate core sample measurements. The reported thermal conductivity value for each sample is an average of three repeated measurements.

Because sediments become stiffer with increasing depth, thermal conductivity measurements were conducted on the split halves. A QTM-500 quick thermal conductivity was utilized to measure hard samples. At the beginning of each half-space thermal conductivity measurement, a 10 cm long split-core piece was taken from the working half of the core and placed in seawater at ambient temperature for 15 min. The sample was then wrapped in stretchable plastic wrap. Care was taken to remove any visible air bubbles between the plastic wrap and the sample surface. The half-space probe was placed on a flat surface of the sample, and heating and measure-

ments were done automatically. Calibration procedures are same as those used for whole-round samples.

Moisture and density measurements

MAD of rocks and sediments were calculated by measuring wet mass, dry mass, and dry volume. Approximately 5 cm³ samples were taken from two intervals (at ~25 and 100 cm from the top of the section as a convention) for each working-half section. For Hole C0002D cores, samples were taken from one interval for each section. In addition, MAD samples were routinely taken from the “cluster” slices next to whole-round samples (except for whole-round samples for microbiology). If the whole-round sampling location overlapped the regular MAD sampling intervals, no additional sample was taken.

In general, care was taken to sample undisturbed parts of the core and to avoid drill mud. Immediately after the samples were collected, wet sediment mass (M_{wet}) was measured. Dry sediment mass (M_{dry}) and volume (V_{dry}) were measured after drying in a convection oven for 24 h at $105^{\circ} \pm 5^{\circ}\text{C}$. Wet and dry masses were weighed using paired electronic balances, which compensated for the ship's heave. Dry volume was measured using a helium-displacement pycnometer (Quantachrome penta-pycnometer) with a nominal precision of ± 0.04 cm³. Measurements were repeated four times and the average of the last three measurements was used. Bulk density, dry density, and density of the solids, as well as porosity and moisture content, were computed, taking into account the precipitation of dissolved salts during drying (Blum, 1997).

Shear strength measurements

Undrained shear strength measurements were determined using a semiautomated laboratory vane shear device (Wykeham Farrance, model WF23544) and a pocket penetrometer (Geotest Instrument Co., model E-284B). Measurements were made at discrete locations on the working halves at a frequency of approximately three per core (at 100 cm from the top of Sections 2, 5, and 7 as a convention). In general, measurements were made adjacent to MAD sampling horizons. Care was taken to conduct tests within undisturbed and homogeneous parts of the core. To minimize disturbance effects resulting from the measurement itself, vane shear tests were generally conducted first, followed by penetrometer tests. Measurements were made with the vane rotation axis and penetrometer penetration direction perpendicular to the split surface.

Vane shear strength $S_{u(v)}$ (kPa) is calculated as

$$S_{u(v)} = T/K_v$$

where

T = torque required to fail the material (N·m) and
 K_v = constant depending on vane dimensions (m³)
 (Blum, 1997).

All measurements reported here were obtained using a vane with height and diameter of 12.7 mm. Failure torque was determined by measuring the degrees of rotation of one of four torsional springs and a linear calibration equation (manufacturer specified) relating the rotation angle to torque for the particular spring being used. Selection of the appropriate spring was based on the anticipated shear strength of the material. Vane shear results were generally considered reliable for shear strength values less than ~150 to 200 kPa, above which excessive cracking and separation of the core material occurred.

The pocket penetrometer provides a measure of unconfined compressive strength in units of kilograms per centimeter squared. Compressive strength is calculated from the penetration resistance generated by pushing a cylindrical probe into the split core surface (Blum, 1997). Penetrometer-based shear strength ($S_{u(p)}$) is calculated as measured compressive strength converted to units of kilopascals and divided by two. Shear strength values reported here were calculated from the average of three penetration trials conducted at adjacent points on the core. Typical spatial separation between trials was on the order of 1 cm. All measurements were obtained using a probe with a nominal diameter of 6.4 mm (0.25 inches). Tests were conducted for shear strength values up to a maximum of ~300 kPa.

MSCL-I: photo image logger

The MSCL-I scans the surface of archive-half cores and creates a digital image. The line-scan camera equips three charge-coupled devices; each charge-coupled device has 1024 arrays. Light reflection from the sample surface passes through the lens and is split into three paths (red, green, and blue) by a beam splitter inside the line-scan camera. Then, each reflection is detected by the corresponding charge-coupled device. Finally, the signals are combined and the digital image is reproduced. Optical distortion downcore is avoided by precise movement of the camera. Spatial resolution is 100 pixels/cm.

MSCL-C: color spectroscopy logger

A color spectrophotometer (Konica-Minolta, CM-2600d) is included on the MSCL-C system. The xyz-

type aluminum frame allows operators to set a maximum of seven core sections on the tray, and the sensor unit (including the spectrophotometer and small distance measuring system using a laser sensor) moves over each section and down at each measurement point to measure the split archive core surface.

Light reflected from the sample surface is collected in the color spectrophotometer's integration sphere. The instrument's structure allows for the specular component to be included (SCI setting) or excluded (SCE setting). The SCE setting is the recommended mode of operation, especially for sediments, to exclude glare. The light is then divided into wavelengths at a 10 nm pitch (400–700 nm), and the spectral sensors in the sphere convert the light to electrical currents proportional to the intensity of the light. Next, the color spectrum from the sample is normalized by the source light of the reflectance. The obtained spectrum is calibrated with the measurement of a pure white standard, which has a high reflectance true value at visible wavelengths and is measured by the vendor, and a black box (zero calibration). Measurements can be calculated based on the 2° or 10° standard observer and any of 11 illuminants.

Color reflectance is categorized as an IODP standard measurement, and the measured color spectrum is normally converted to L^* , a^* , and b^* parameters. L^* , a^* , and b^* provide relative changes in the composition of the bulk material and are widely used to correlate sections from core to core or hole to hole and to analyze the characteristic and cyclicity of lithologic changes.

Anisotropies of *P*-wave velocity and electrical resistivity

Three directional measurements on discrete samples of *P*-wave velocity and electrical conductivity were performed on RCB cores. Core pieces were cut with a saw equipped with two parallel disks set at 20 mm spacing. This sample preparation enables measurement of both electrical conductivity and *P*-wave anisotropies. If the core has no (or subhorizontal) apparent stratification or foliation, cubes are cut with faces 1, 2, and 3 orthogonal to the x -, y - and z -axes of the core reference, respectively. Orientation of the axes is the same as for paleomagnetism, with z -pointing down along the core axis, x -pointing into the working half, and y - in the core face.

The sample is held between two stainless steel electrodes covered with filters soaked in seawater and the complex impedance ($R + jX$) is measured at 10 kHz between opposite cube faces with an Agilent 4263B component analyzer. Three such measure-

ments may be performed along directions x , y , and z . The conductance tensor component (e.g., σ_x) along a given direction (e.g., x) is computed from the impedance measured along this direction and sample dimensions according to the formula

$$\sigma_x = (L_x/L_y L_z)[(R_x - R_0) - j(X_x - X_0)/(R_x - R_0)^2 + (X_x - X_0)^2],$$

where L is the length and R_0 and X_0 refer to the measured impedance of the filter. Conductance tensor components σ_y and σ_z are obtained by substitution in this formula.

To measure P -wave velocity along a given direction, the sample is held with a force of 49 N (corresponding to a pressure of 120 kPa) between two transducers covered with rubber spacers. The emitter is connected to a pulse generator (Physical Acoustics C-101-HV); the receiver is connected to an oscilloscope synchronized with the pulse generator. The oscilloscope signal is transferred to a computer, and the arrival time is picked and logged automatically. This setup has a delay of 2.10 μ s, which is subtracted from the arrival time to obtain the travel time. The velocity along a given direction is simply given by the length divided by the travel time.

When three measurements are performed, the orientation of the tensor cannot be known. However, some simplification may be expected if the sample is almost transversely anisotropic around the axis perpendicular to the main foliation or stratification. The two following definitions appear convenient and are given here with electrical conductivity as example. Apparent anisotropy in the horizontal plane is

$$\alpha_t = 2[(\sigma_x - \sigma_y)/(\sigma_x + \sigma_y)].$$

Apparent transverse anisotropy is

$$\alpha_T = \{[(\sigma_x + \sigma_y)/2] - \sigma_z\} / \{[(\sigma_x + \sigma_y)/2] + \sigma_z\}$$

for a truly transversely anisotropic medium, and in the core reference frame (x , y , and z) the anisotropy ratio $\alpha = \alpha_t/\alpha_T$ is a function of the dip of the foliation in the sample.

In situ temperature measurement

In situ temperature measurement was carried out using the advanced piston coring temperature tool (APCT3) (Fig. F20), which is the third-generation tool of its kind used with the HPCS to measure downhole in situ temperatures. The APCT3 consists of three components: electronics, coring hardware, and software. During this expedition, in situ temperature measurement was basically done for every third core during HPCS coring in Holes C0001E and

C0001F from 13.60 to 170.98 m CSF and in Hole C0002D from 15.38 to 158.97 m CSF. The sensor was calibrated for a working range of 0°–45°C.

The electronics fit into a special cutting shoe, which was lowered to the seafloor and shot into the formation. To equilibrate with seafloor temperature, the cutting shoe was held at the mudline for ~5–10 min before penetration. After shooting, it takes ~10 min for the sensor to equilibrate to the in situ temperature of the formation. Mud pumps need to be off during temperature equilibration. Shooting the barrel into the formation normally causes a rapid increase in temperature due to frictional heating. After that, temperature decreases with time along a decay curve. Temperature was measured as a time series with a sampling rate of 1 s. Temperature data were logged onto a microprocessor within the downhole tool; when the tool was retrieved, data were downloaded to the computer.

A typical penetration curve exists of three parts: a rise in temperature at the beginning due to frictional heating, a decay curve as the sensor equilibrates to the in situ temperature of the sediment, and another rise while pulling the tool out (Fig. F21). In situ temperature was calculated by using the decay curve after penetration. Therefore, the interval used for calculation was not disturbed, for example, by vibration that causes frictional heating. Data were processed using the program TP-Fit, which runs on Matlab. The theoretical background of the program was provided by M. Heeseman (pers. comm., 2007). In situ temperatures could be calculated by using the decay curve.

Core-log-seismic integration

No logging was done during Expedition 315. The integration of LWD data with seismic reflection data at sites drilled during Expedition 315 was done during Expedition 314. Reference seismic profiles are prestack depth-migrated lines from the Center for Deep Earth Exploration (CDEX) 3-D block. Depths in the seismic line were fitted to LWD check shot data provided by the Expedition 314 Scientists, and we will rely on their work.

Integration of cores with LWD data relies primarily on lithologic boundaries, magnetic susceptibility, and NGR MSCL data. Details about MSCL measurements are described in “**Physical properties.**” Magnetic susceptibility data were used for correlation between cores from different holes at the same site. NGR data were used for correlation between the cores and the log. The LWD geoVISION resistivity tool was used at Sites C0001 and C0002 and comprises NGR and resistivity measurement and imag-

ery. Sonic log slowness data, gamma ray density, and neutron porosity are available from the other tools used and may also be compared with MSCL measurements on cores or with measurements on discrete samples (MAD and *P*-wave velocity measurements; see “**Physical properties**” for details). Core low-field magnetic susceptibility and NGR emissions were measured with the MSCL on whole-round sections every 4 cm and every 15 or 16 cm, respectively. The magnetic susceptibility core log was of good quality overall and was filtered for voids and disturbed intervals according to the core density from gamma ray attenuation MSCL-W measurements. On HPCS and ESCS cores, magnetic susceptibility measurements made at intervals with measured density <1500 kg/m³ (70% porosity) were discarded. On RCB cores, the threshold was set to 1600 kg/m³ (65% porosity).

Mechanical difficulties prevented systematic NGR measurements on whole-round cores. Measurements on the archive half after splitting yield data with a higher noise level, but these data are still usable as a correlation tool. The unit of the MSCL-W gamma emission data is counts per second, and the only calibration is an ambient noise measurement (~40 cps for MSCL-W). Values below 15 cps (or 55 cps before noise correction) were discarded because they often correspond to voids. Assuming the liner has negligible radioactivity, the ambient noise level should be the same when measuring the whole-round core or the archive half. Considering the symmetry of the gamma ray counting system, which comprises four detectors at 90° angles, the number of counts from the half core should be half the number of counts from the whole-round cores. Comparison of data acquired on the same cores shows that applying a 38 cps ambient noise correction and a corrective factor of two to the archive half counts yields results consistent with measurements on whole-round cores (Fig. F22).

LSF is the depth reference. There are two definitions of core depth. In the standard definition of CSF (IODP Method A), the depth in the core is added to the depth of the drill bit at the beginning of coring. This definition leads to overlaps between expanded HPCS cores and, sometimes, between RCB cores when drilling fluid and/or cuttings enter the core barrel. The compressed core depth below seafloor (CSF-B; IODP Method B) is also given by J-CORES and corrects the discrepancy between the length of expanded cores and the advance of the drill bit by applying an arbitrary linear correction over the whole length of core. The correlation between core depth below seafloor and LWD depth below seafloor is based on this depth (rather than the Method A depth). Depth transfer functions are defined by lin-

ear regression between correlated peaks. Cores with <5 m of recovery do not generally provide useful constraints. On intervals with better recovery, several peak-to-peak correlations can sometimes be done within a single RCB core, and the Method B core depth log appears condensed by 5% to 30% with respect to LWD data. This indicates that partial recovery can spread over most of the cored interval, in contrast to the assumptions of the Method A depth definition.

References

- Angelier, J., 1994. Fault slip analysis and palaeostress reconstruction. In Hancock, P.L. (Ed.), *Continental Deformation*: Tarrytown, NY (Pergamon Press), 53–100.
- Berggren, W.A., Hilgen, F.J., Langereis, C.G., Kent, D.V., Obradovich, J.D., Raffi, I., Raymo, M.E., and Shackleton, N.J., 1995. Late Neogene chronology: new perspectives in high-resolution stratigraphy. *Geol. Soc. Am. Bull.*, 107(11):1272–1287. doi:10.1130/0016-7606(1995)107<1272:LNCNPI>2.3.CO;2
- Blow, W.H., 1969. Late middle Eocene to Recent planktonic foraminiferal biostratigraphy. In Brönnimann, P., and Renz, H.H. (Eds.), *Proc. First Int. Conf. Planktonic Microfossils, Geneva, 1967*: Leiden (E.J. Brill), 1:199–422.
- Blum, P., 1997. Physical properties handbook: a guide to the shipboard measurement of physical properties of deep-sea cores. *ODP Tech. Note*, 26. doi:10.2973/odp.tn.26.1997
- Brothers, R.J., Kemp, A.E.S., and Maltman, A.J., 1996. Mechanical development of vein structures due to the passage of earthquake waves through poorly consolidated sediments. *Tectonophysics*, 260(4):227–244. doi:10.1016/0040-1951(96)00088-1
- Cowan, D.S., 1982. Origin of “vein structure” in slope sediments on the inner slope of the Middle America Trench off Guatemala. In Aubouin, J., von Huene, R., et al., *Init. Repts. DSDP*, 67: Washington, DC (U.S. Govt. Printing Office), 645–650. doi:10.2973/dsdp.proc.67.132.1982
- Cranston, R.E., 1991. Testing a higher resolution interstitial-water method for the Ocean Drilling Program. In Barron, J., Larsen, B., et al., *Proc. ODP, Sci. Results*, 119: College Station, TX (Ocean Drilling Program), 393–399. doi:10.2973/odp.proc.sr.119.173.1991
- Fisher, A.T., and Underwood, M.B., 1995. Calibration of an X-ray diffraction method to determine relative mineral abundances in bulk powders using matrix singular value decomposition: a test from the Barbados accretionary complex. In Shipley, T.H., Ogawa, Y., Blum, P., et al., *Proc. ODP, Init. Repts.*, 156: College Station, TX (Ocean Drilling Program), 29–37. doi:10.2973/odp.proc.ir.156.103.1995
- Fuller, M., 1969. Magnetic orientation of borehole cores. *Geophysics*, 34(5):772–774.
- GE Healthcare, 2006. *LightSpeed Series Learning and Reference Guide-Multi Slice CT*: Waukesha, Wisconsin (GE Healthcare), 936.

- Gradstein, F.M., Ogg, J.G., and Smith, A. (Eds.), 2004. *A Geologic Time Scale 2004*: Cambridge (Cambridge Univ. Press). <http://www.stratigraphy.org/>
- Hanken, N.-M., 1979. The use of sodium tetraphenylborate and sodium chloride in the extraction of fossils from shales. *J. Paleontol.*, 53(3):738–741.
- Hulme, S.M., Wheat, C.G., Coggon, R.M., and McManus, J., 2008. Data report: trace element, Sr isotope, and Ge/Si composition of fluids and sediments in ridge-flank low-temperature hydrothermal environments. In Fisher, A.T., Urabe, T., Klaus, A., and the Expedition 301 Scientists, *Proc. IODP, 301*: College Station, TX (Integrated Ocean Drilling Program Management International, Inc.). [doi:10.2204/iodp.proc.301.202.2008](https://doi.org/10.2204/iodp.proc.301.202.2008)
- Kodama, K.P., 1984. Palaeomagnetism of granitic intrusives from the Precambrian basement under eastern Kansas: orienting drill cores using secondary magnetization components. *Geophys. J. R. Astron. Soc.*, 76:273–287.
- Li, B., Jian, Z., Li, Q., Tian, J., and Wang, P., 2005. Paleooceanography of the South China Sea since the middle Miocene: evidence from planktonic foraminifera. In Wang, P., and Lipps, J. (Eds.), *Marine Micropaleontology of the South China Sea*. *Mar. Micropaleontol.*, 54(1–2):49–62. [doi:10.1016/j.marmicro.2004.09.003](https://doi.org/10.1016/j.marmicro.2004.09.003)
- Lourens, L.J., Hilgen, F.J., Laskar, J., Shackleton, N.J., and Wilson, D., 2004. The Neogene period. In Gradstein, F.M., Ogg, J., et al. (Eds.), *A Geologic Time Scale 2004*: Cambridge (Cambridge Univ. Press), 409–440. <http://www.stratigraphy.org/>
- Lunau, M., Lemke, A., Walther, K., Martens-Habben, W., and Simon, M., 2005. An improved method for counting bacteria from sediments and turbid environments by epifluorescence microscopy. *Environ. Microbiol.*, 7(7):961–968. [doi:10.1111/j.1462-2920.2005.00767.x](https://doi.org/10.1111/j.1462-2920.2005.00767.x)
- Manheim, F.T., 1966. A hydraulic squeezer for obtaining interstitial waters from consolidated and unconsolidated sediments. *Geol. Surv. Prof. Pap. (U.S.)*, 550-C:256–261.
- Martini, E., 1971. Standard Tertiary and Quaternary calcareous nannoplankton zonation. In Farinacci, A. (Ed.), *Proc. Second Planktonic Conf., Roma, 1970*: Rome (Ed. Tecnosci.), 2:739–785.
- Mazzullo, J., and Graham, A.G. (Eds.), 1988. Handbook for shipboard sedimentologists. *ODP Tech. Note*, 8. [doi:10.2973/odp.tn.8.1988](https://doi.org/10.2973/odp.tn.8.1988)
- Mazzullo, J.M., Meyer, A., and Kidd, R.B., 1988. New sediment classification scheme for the Ocean Drilling Program. In Mazzullo, J.M., and Graham, A.G. (Eds.), *Handbook for Shipboard Sedimentologists*. *ODP Tech. Note*, 8:45–67. [doi:10.2973/odp.tn.8.1988](https://doi.org/10.2973/odp.tn.8.1988)
- McFadden, P.L., and Reid, A.B., 1982. Analysis of paleomagnetic inclination data. *Geophys. J. R. Astron. Soc.*, 69:307–319.
- Mees, F., Swennen, R., Van Geet, M. and Jacobs, P., 2003. Applications of X-ray computed tomography in the geosciences. *Geol. Soc. Spec. Publ.*, 215(1):1–6. [doi:10.1144/GSL.SP.2003.215.01.01](https://doi.org/10.1144/GSL.SP.2003.215.01.01)
- Motoyama, I., Niitsuma, N., Maruyama, T., Hayashi, H., Kamikuri, S., Shiono, M., Kanamatsu, T., Aoki, K., Morishita, C., Hagino, K., Nishi, H., and Oda, M., 2004. Middle Miocene to Pleistocene magneto-biostratigraphy of ODP Sites 1150 and 1151, northwest Pacific: sedimentation rate and updated regional geological timescale. *Isl. Arc*, 13(1):289–305. [doi:10.1111/j.1440-1738.2003.00426.x](https://doi.org/10.1111/j.1440-1738.2003.00426.x)
- Nakano, T., Nakashima, Y., Nakamura, K., and Ikeda, S., 2000. Observation and analysis of internal structure of rock using X-ray CT. *Chishitsugaku Zasshi*, 106(5):363–378.
- Oda, M., 1977. Planktonic foraminiferal biostratigraphy of the Late Cenozoic sedimentary sequence, central Honshu, Japan. *Sci. Rep. Tohoku Univ., Ser. 2*, 48(1–2):1–76.
- Ogawa, Y., 1980. Beard-like veinlet structure as fracture cleavage in the Neogene siltstone in the Miura and Boso Peninsulas, central Japan. *Kyushu Daigaku Rigakubu Kenkyu Hokoku, Chishitsugaku*, 13(2):321–327.
- Okada, H., and Bukry, D., 1980. Supplementary modification and introduction of code numbers to the low-latitude coccolith biostratigraphic zonation (Bukry, 1973; 1975). *Mar. Micropaleontol.*, 5:321–325. [doi:10.1016/0377-8398\(80\)90016-X](https://doi.org/10.1016/0377-8398(80)90016-X)
- Parés, J.M., Hassold, N.J.C., Rea, D.K., and van der Pluijm, B.A., 2007. Paleocurrent directions from paleomagnetic reorientation of magnetic fabrics in deep-sea sediments at the Antarctic Peninsula Pacific margin (ODP Sites 1095, 1101). *Mar. Geol.*, 242(4):261–269. [doi:10.1016/j.margeo.2007.04.002](https://doi.org/10.1016/j.margeo.2007.04.002)
- Parés, J.M., Schleicher, A.M., van der Pluijm, B., and Hickman, S., in press. Paleomagnetic reorientation of San Andreas Fault Observatory at Depth (SAFOD) core. *Geophys. Res. Lett.*
- Petit, J.P., 1987. Criteria for the sense of movement on fault surfaces in brittle rocks. *J. Struct. Geol.*, 9(5–6):597–608. [doi:10.1016/0191-8141\(87\)90145-3](https://doi.org/10.1016/0191-8141(87)90145-3)
- Pimmel, A., and Claypool, G., 2001. Introduction to shipboard organic geochemistry on the *JOIDES Resolution*. *ODP Tech. Note*, 30. [doi:10.2973/odp.tn.30.2001](https://doi.org/10.2973/odp.tn.30.2001)
- Raffi, I., Backman, J., Fornaciari, E., Pálfi, H., Rio, D., Lourens, L., and Hilgen, F., 2006. A review of calcareous nannofossil astrochronology encompassing the past 25 million years. *Quat. Sci. Rev.*, 25(23–24):3113–3137. [doi:10.1016/j.quascirev.2006.07.007](https://doi.org/10.1016/j.quascirev.2006.07.007)
- Richter, C., Acton, G., Endris, C., and Radsted, M., 2007. Handbook for shipboard paleomagnetists. *ODP Tech. Note*, 34. [doi:10.2973/odp.tn.34.2007](https://doi.org/10.2973/odp.tn.34.2007)
- Rothwell, R.G., 1989. *Minerals and Mineraloids in Marine Sediments: An Optical Identification Guide*: London, UK (Elsevier).
- Shepard, F.P., 1954. Nomenclature based on sand-silt-clay ratios. *J. Sediment. Petrol.*, 24(3):151–158.
- Shibuya, H., Merrill, D.L., Hsu, V., and Leg 124 Shipboard Scientific Party, 1991. Paleogene counterclockwise rotation of the Celebes Sea—orientation of ODP cores utilizing the secondary magnetization. In Silver, E.A., Rangin, C., von Breyman, M.T., et al., *Proc. ODP, Sci. Results*, 124: College Station, TX (Ocean Drilling Program), 519–523. [doi:10.2973/odp.proc.sr.124.169.1991](https://doi.org/10.2973/odp.proc.sr.124.169.1991)
- Smith, D.C., Spivack, A.J., Fisk, M.R., Haveman, S.A., and Staudigel, H., 2000. Tracer-based estimates of drilling-

- induced microbial contamination of deep sea crust. *Geomicrobiol. J.*, 17(3):207–219. doi:10.1080/01490450050121170
- Tauxe, L., 1998. *Paleomagnetic Principles and Practice*: Dordrecht, Netherlands (Kluwer Academic).
- Tauxe, L., Tucker, P., Peterson, N.P., and LaBrecque, J.L., 1984. Magnetostratigraphy of Leg 73 sediments. In Hsü, K.J., LaBrecque, J.L., et al., *Init. Repts. DSDP, 73*: Washington, DC (U.S. Govt. Printing Office), 609–621. doi:10.2973/dsdp.proc.73.123.1984
- Thompson, P.R., Bé, A.W.H., Duplessy, J.-C., and Shackleton, N.J., 1979. Disappearance of pink-pigmented *Globigerinoides ruber* at 120,000 yr BP in the Indian and Pacific oceans. *Nature (London, U. K.)*, 280(5723):554–558. doi:10.1038/280554a0
- Underwood, M.B., Basu, N., Steurer, J., and Udas, S., 2003. Data report: normalization factors for semiquantitative X-ray diffraction analysis, with application to DSDP Site 297, Shikoku Basin. In Mikada, H., Moore, G.F., Taira, A., Becker, K., Moore, J.C., and Klaus, A. (Eds.), *Proc. ODP, Sci. Results, 190/196*: College Station, TX (Ocean Drilling Program), 1–28. doi:10.2973/odp.proc.sr.190196.203.2003
- Wheat, C.G., Boulègue, J., and Mottl, M.J., 1994. A technique for obtaining pore water chemical composition from indurated and hydrothermally altered sediment and basalt: the ground rock interstitial normative determination (grind). In Mottl, M.J., Davis, E.E., Fisher, A.T., and Slack, J.F. (Eds.), *Proc. ODP, Sci. Results, 139*: College Station, TX (Ocean Drilling Program), 429–437. doi:10.2973/odp.proc.sr.139.234.1994
- Young, J.R., 1999. Neogene. In Bown, P.R. (Ed.), *Calcareous Nannofossil Biostratigraphy*: Dordrecht, The Netherlands (Kluwer Academic), 225–265.

Publication: 5 March 2009
MS 315-122

Figure F1. OsiriX screen shot of core with high gas content. Gas-filled voids appear as black vesicular texture (Section 315-C0001F-18H-1).

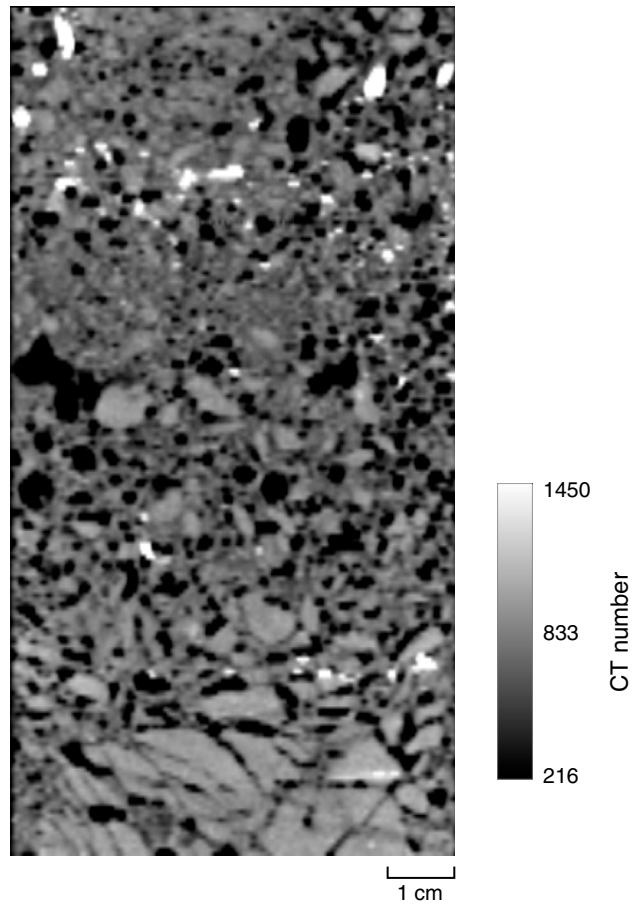


Figure F2. OsiriX screen shot of drilling-induced “biscuits” (Section 315-C0001F-20X-1).

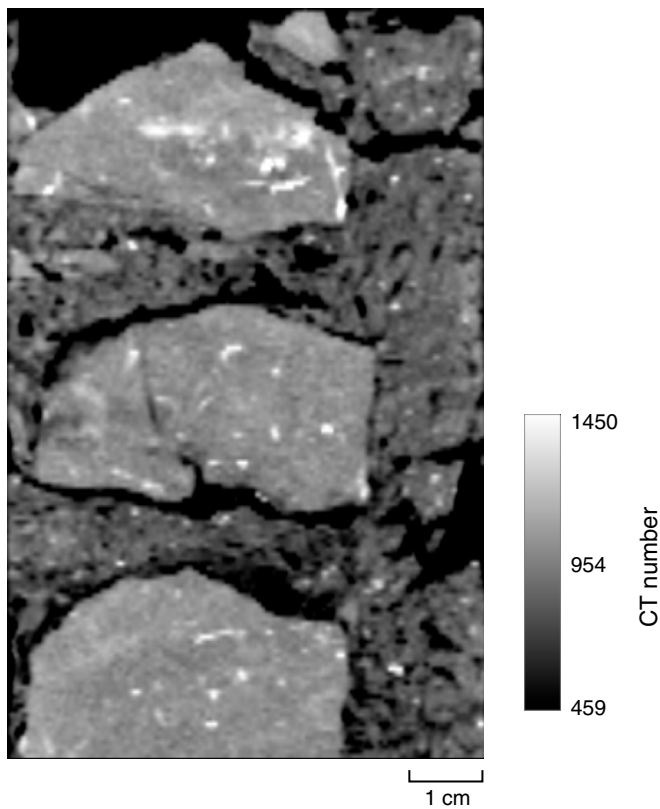




Figure F3. Sample structural geology CT log sheet.

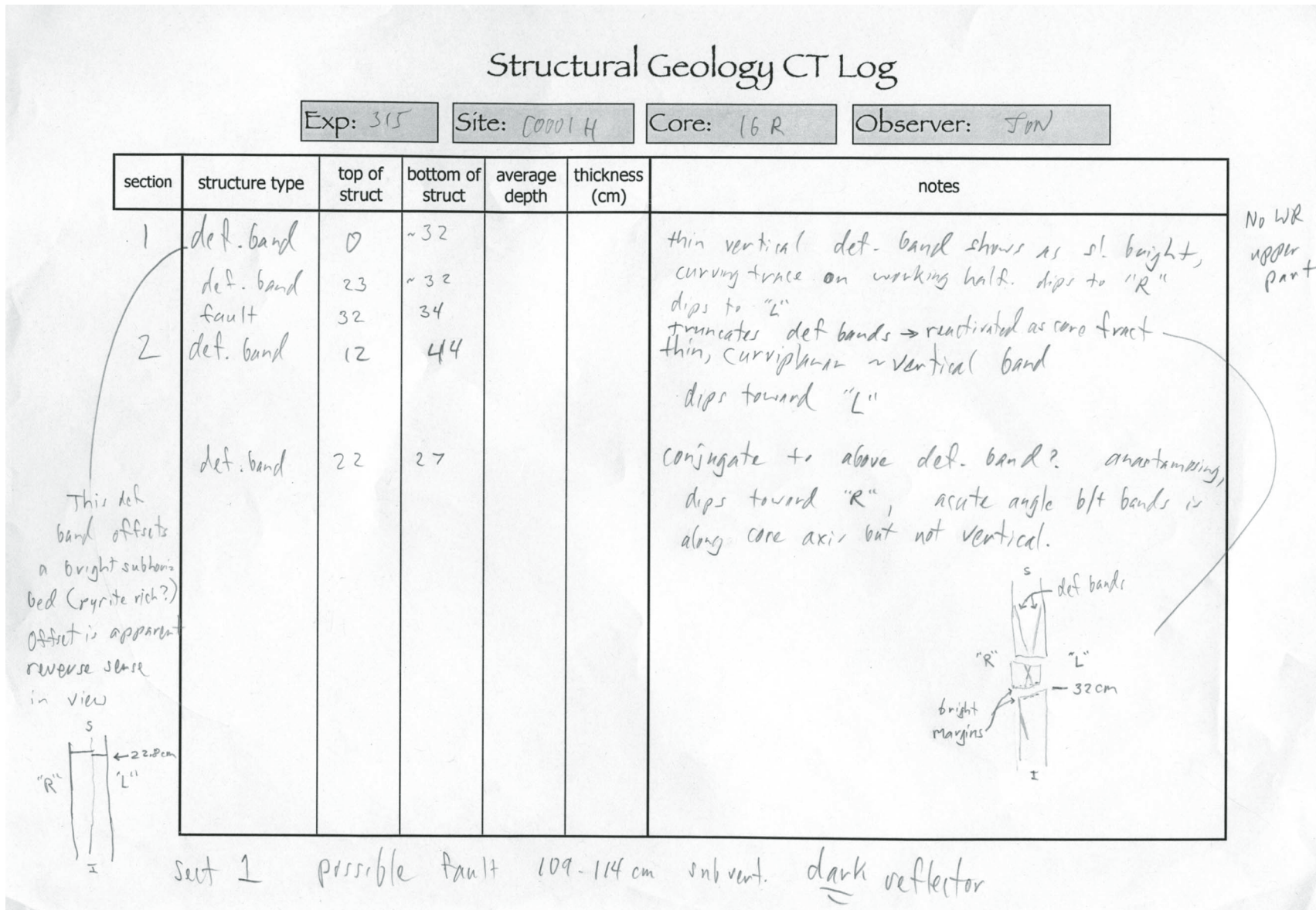


Figure F5. Diffractograms of mixtures of standard minerals showing positions of diagnostic X-ray diffraction peaks used to calculate relative mineral abundances. Cl = total clay minerals, Q = quartz, P = plagioclase, Cc = calcite.

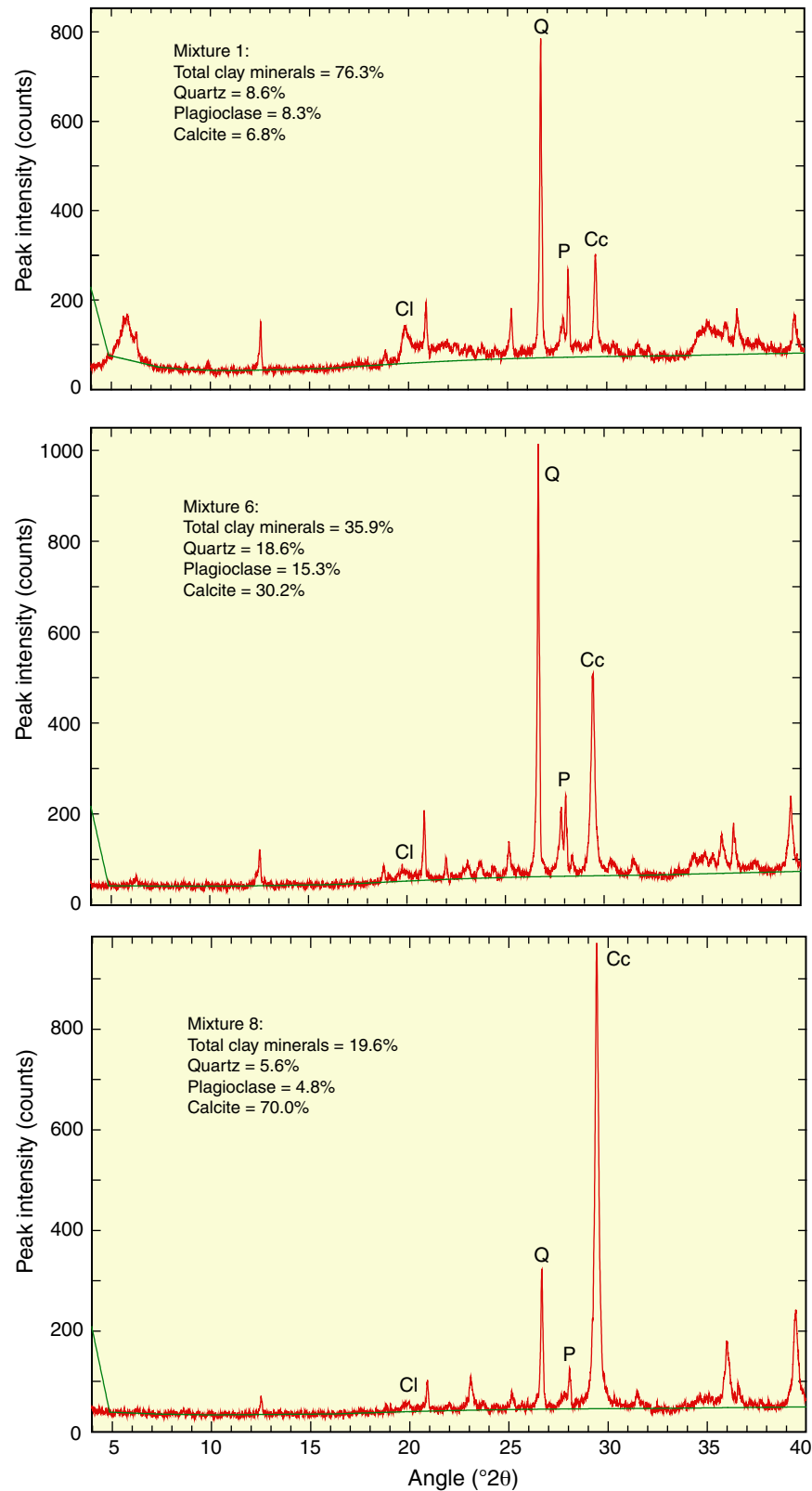


Figure F6. Modified protractor used to measure apparent dips, trends, plunges, and rakes on planar and linear features in a split core.

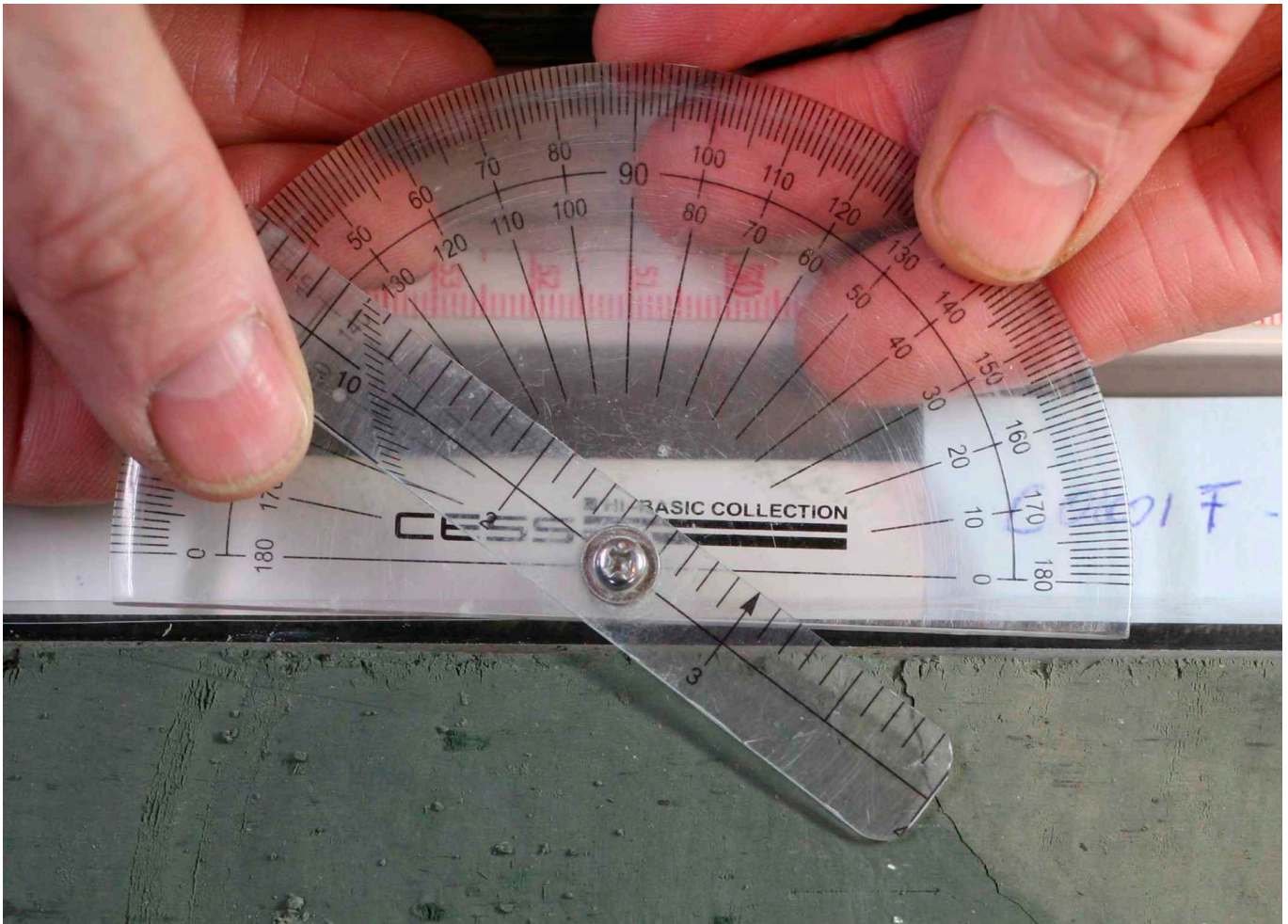




Figure F7. Sample log sheet used to record structural data and observations from working half of split core.

Structural Geology

Exp: 315 Site: C0001E Core: 8H Observer: Summary:



section	structure ID	top of struct	bottom of struct	average depth	thickness (cm)	core face app. dip		2nd app. dip		orientation		orientation		coherent interval (for P-)		P-mag pole		corrected orientation		notes
						az.	dip	az.	dip	strike	dip	dip dir	dip	top	bottom	az/trend	dip	az/trend	dip	
	Bedding	95.8	97		1.2	270	1	0	2					85	100					dark gray clay layer with a diffuse top and a sharp base contact with 0.5 cm thick greenish clay layer
	Normal fault	50	67			270	69	16	0					24.5	55.5					 <p>dark gray clay apparent offset greenish clay</p>
	Bedding	36	37		0.5	90	3	180	5					25	40					greenish clay layer
	Bedding	9	14		5.0	090	06	180	0					0	23					graded ash bed somewhat irreg basal contact
	Bedding	79	80		0.3	270	5	0	8					60	101					silty layer
	Vein structure	80	89																	 <p>vein structure</p> <p>normal fault</p>
	Normal fault	89	100			90	73	320	0											
	4	92	108			90	69	315	0											



Figure F8 (continued).

coherent interval (for P-mag)		P-mag pole		corrected orientation (RHR)			fault		notes
top	bottom	Dec	Inc	dip dir	strike	dip	str rake	slip sense	
115	140	295.1	35	316	226	79	90	T	brecciated throughout the section and wet; clast size: several mm to several cm; largely missing at 110–130 cm
0	140	270.3	-5.6	180	90	90	90	T	anastomosing; 2.1 cm offset of two zoophycos layers
0	140	270.3	-5.6	238	148	79	90	N	continued from section 1; wall rock fragments in the fault zone
0	140	270.3	-5.6	360	270	4	90	N	anastomosing; offset of a zoophycos layer
0	140	270.3	-5.6	45	315	7			worm tubes sheared; ≈1mm thick sharp planar base
0	106			233	143	68	90	N	dark gray clay layer
0	106			129	39	80	73	N	somewhat irregular dark gray band; likely a conjugate set with the fault below
107	141			90	0	16	88		≈0.8 cm offset of a greenish layer
107	141			52	322	75	90	N	sharp planar black band with slickenside
107	141			255	165	40	109	T	top truncated by another fault; boundary between bioturbated and non-bioturbated beds
107	141			107	17	10	81	T	slip sense based on slickensteps
0	30			69	339	68	90	N	likely a conjugate set with the above fault
31	96			29	299	83	92	N	continued from section 3; likely layer offset
104	140			275	185	6	90	T	1.7 cm offset of a zoophycos layer
104	140			272	182	3			worm tubes sheared
104	140								cut by the above shear zone
85	146			318	228	77			trace fossils truncated; maybe related with dewatering
85	146			270	180	90			upper portion of the above band
				270	180	90			
				270	180	90			
				270	180	90			
				270	180	90			
				270	180	90			

Red means inverse polarity P-mag

Green means interpolated P-mag from upper & lower sections

Figure F9. Core reference frame and x -, y -, and z -coordinates used in orientation data calculations.

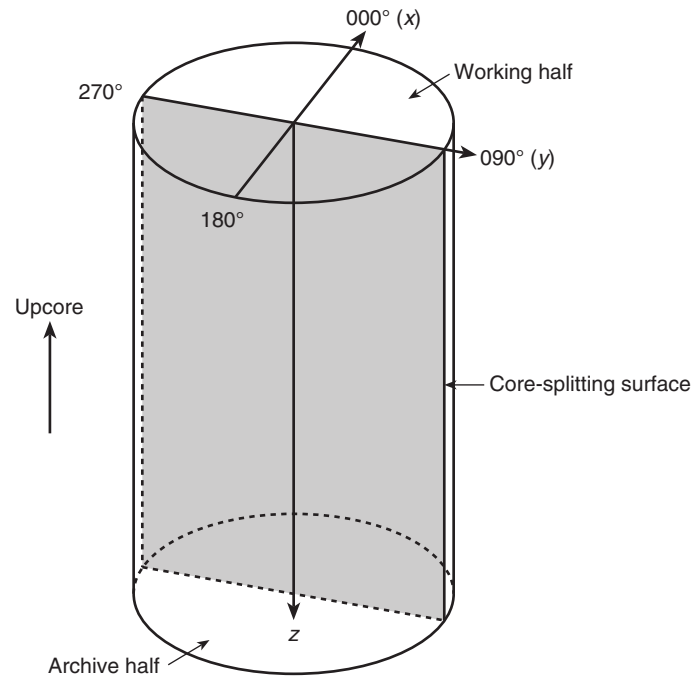


Figure F10. Calculation of plane orientation (shaded) from two apparent dips represented by unit vectors v_1 and v_2 . v_1 and v_2 parallel the intersections of the plane of interest with two auxiliary planes, the split core surface and an imaginary plane perpendicular to the split core surface and parallel to the core axis. (α_1, β_1) and (α_2, β_2) = trends and plunges v_1 and v_2 in core reference frame. v_n = unit vector normal to plane.

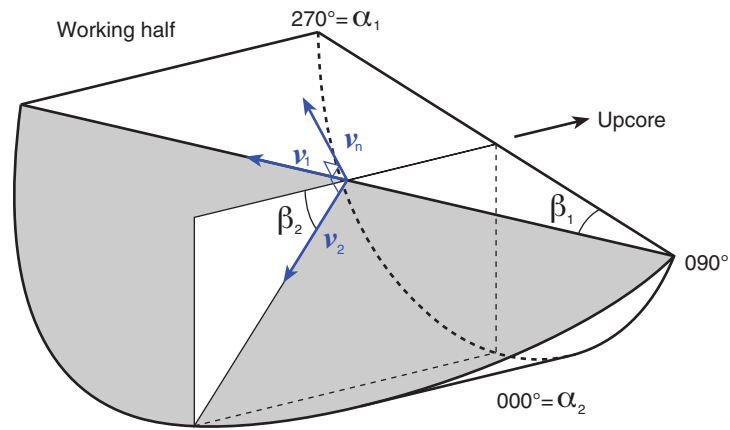


Figure F11. Dip direction (α_d), right-hand rule strike (α_s), and dip (β) of a plane deduced from its normal azimuth (α_n) and dip (β_n). **A.** $\beta_n < 0^\circ$. **B.** $\beta_n \pm 0^\circ$. v_n = unit vector normal to plane.

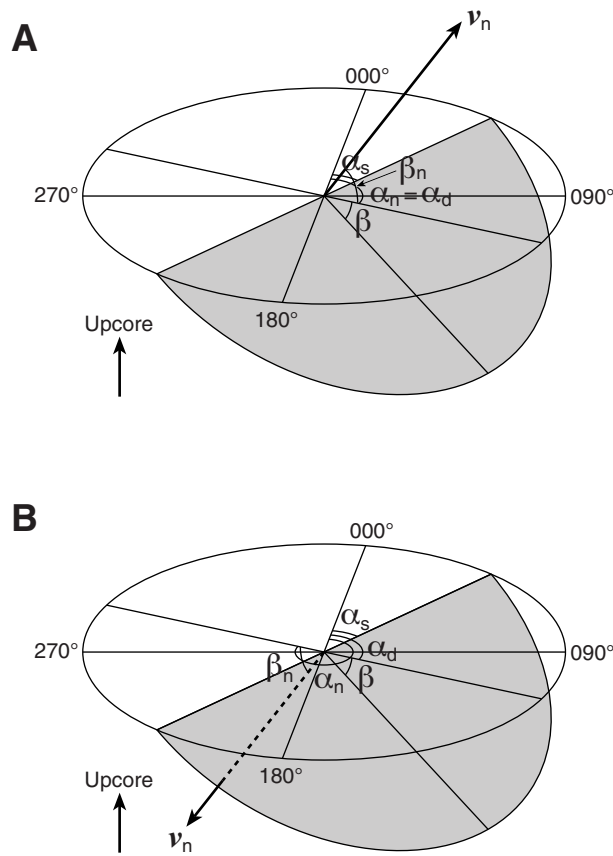


Figure F12. Apparent rake measurement of slickenlines on a fault surface from 270° direction of split-core surface trace. ϕ_a = apparent rake, v_n = unit vector normal to fault plane, v_c = unit vector normal to split core surface, v_i = unit vector parallel to intersection line between fault plane and split core surface.

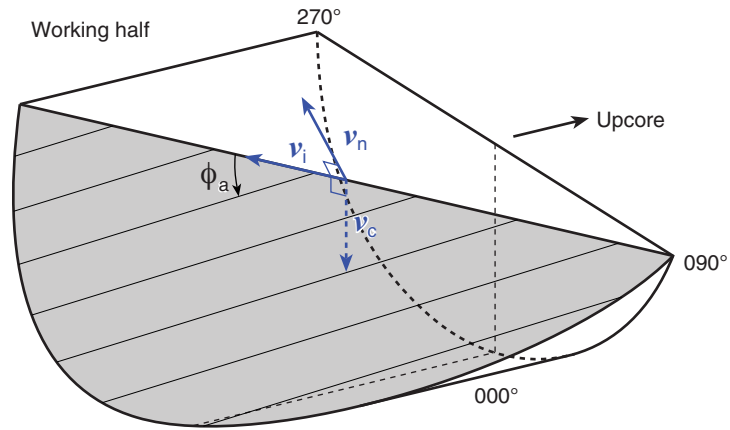


Figure F13. Rake of slickenlines (ϕ) deduced from rake of intersection line between fault plane and split-core surface (ϕ_i) and apparent rake measured (ϕ_a). **A.** Apparent rake measured from top or 090° direction when fault plane dips toward west. **B.** Apparent rake measured from bottom or 090° direction when fault plane dips toward east. **C.** Apparent rake measured from top or 270° direction when fault plane dips toward east. **D.** Apparent rake measured from bottom or 270° direction when fault plane dips toward west. α_s = right-hand rule strike of fault plane, v_n = unit vector normal to fault plane; v_c = unit vector normal to split core surface; v_i = unit vector parallel to intersection line between fault plane and split core surface.

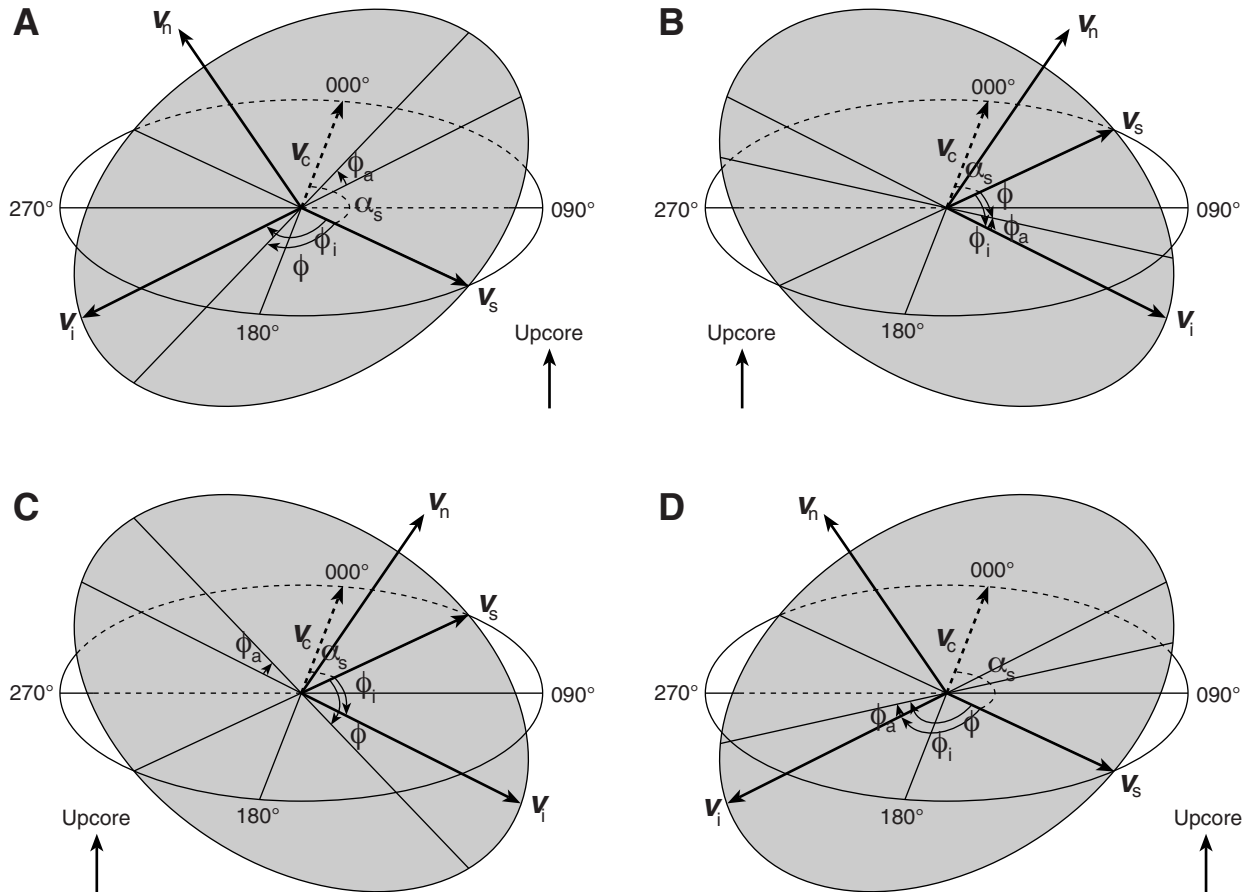


Figure F14. Azimuth correction based on paleomagnetic data. **A.** Paleomagnetic inclination $\beta_p \pm 0^\circ$. **B.** Paleomagnetic inclination $\beta_p < 0^\circ$. α_p = paleomagnetic declination, α_d and α_s = dip direction and right-hand-rule strike of plane.

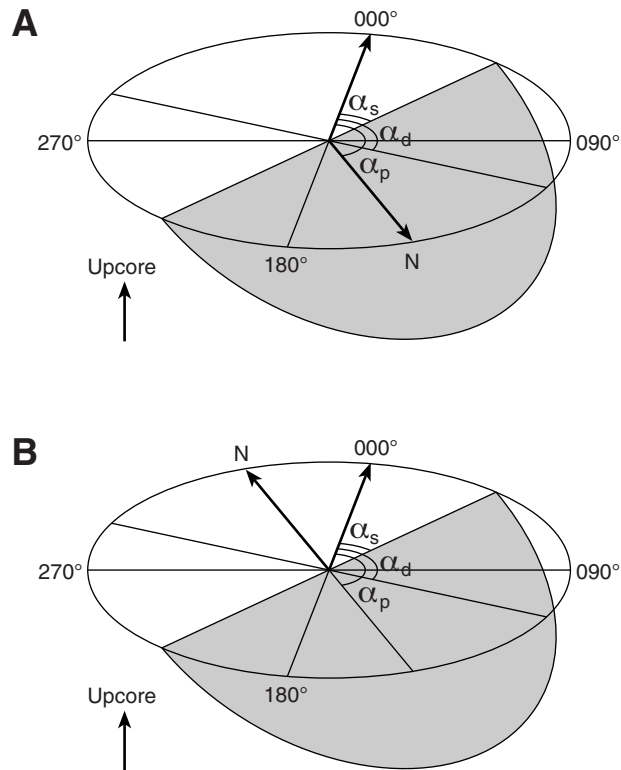


Figure F15. Structural geology window in J-CORES visual core description program. Fault data are entered two ways: fault and slickenline data separately or fault data including slickenline parameters as a comment.

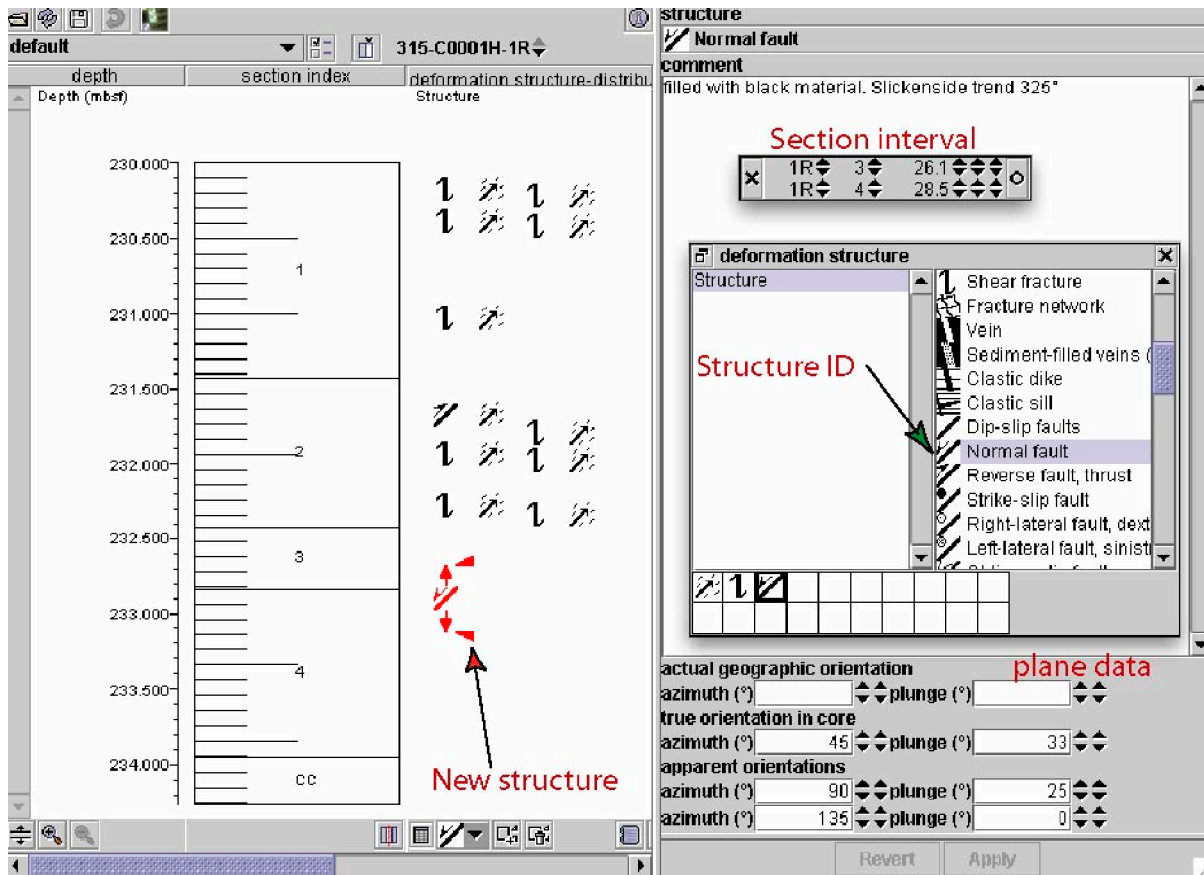


Figure F16. Overview of Cenozoic era magnetostratigraphic and biostratigraphic events. FO = first occurrence, LO = last occurrence. Black = normal polarity, white = reversed polarity.

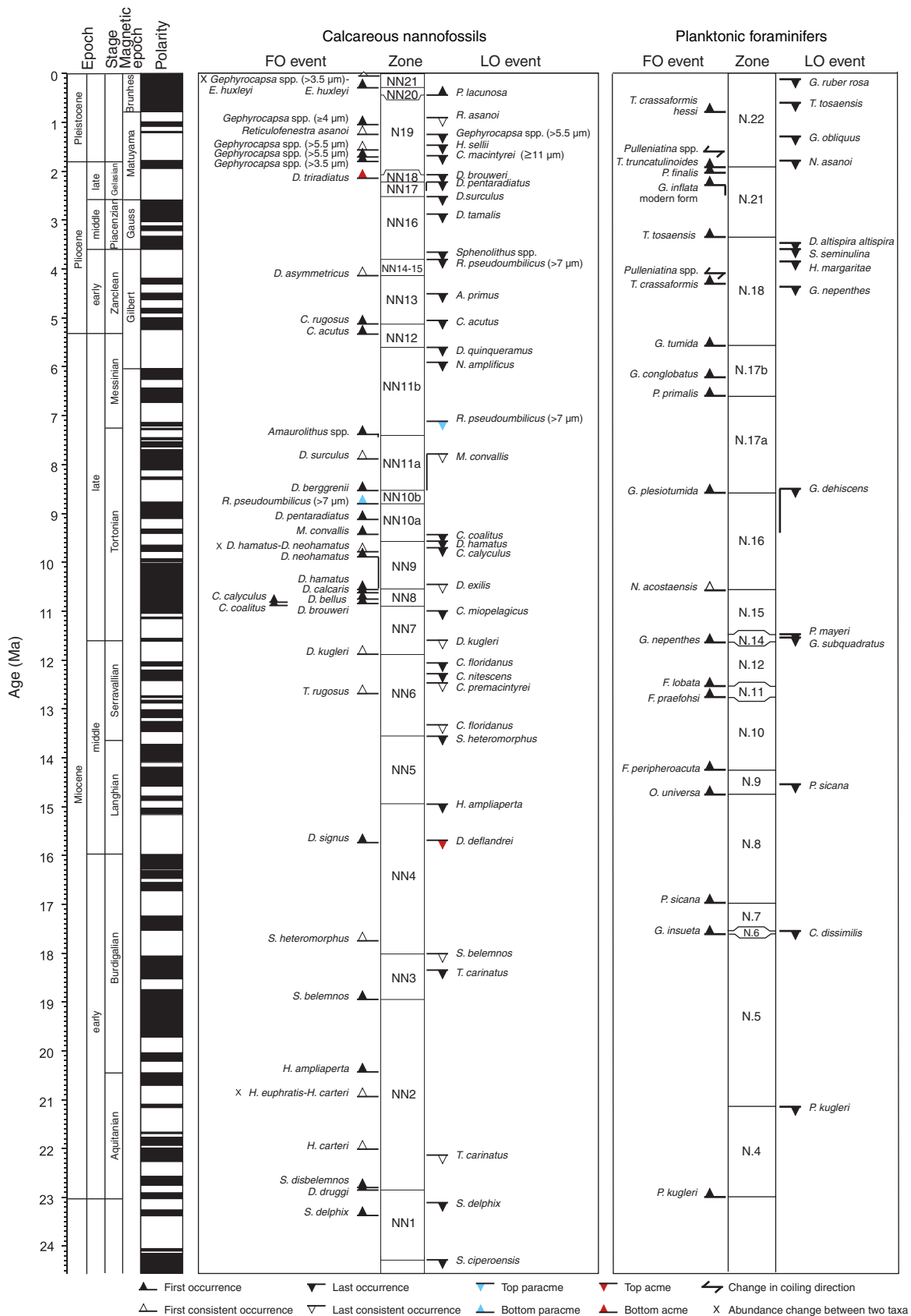


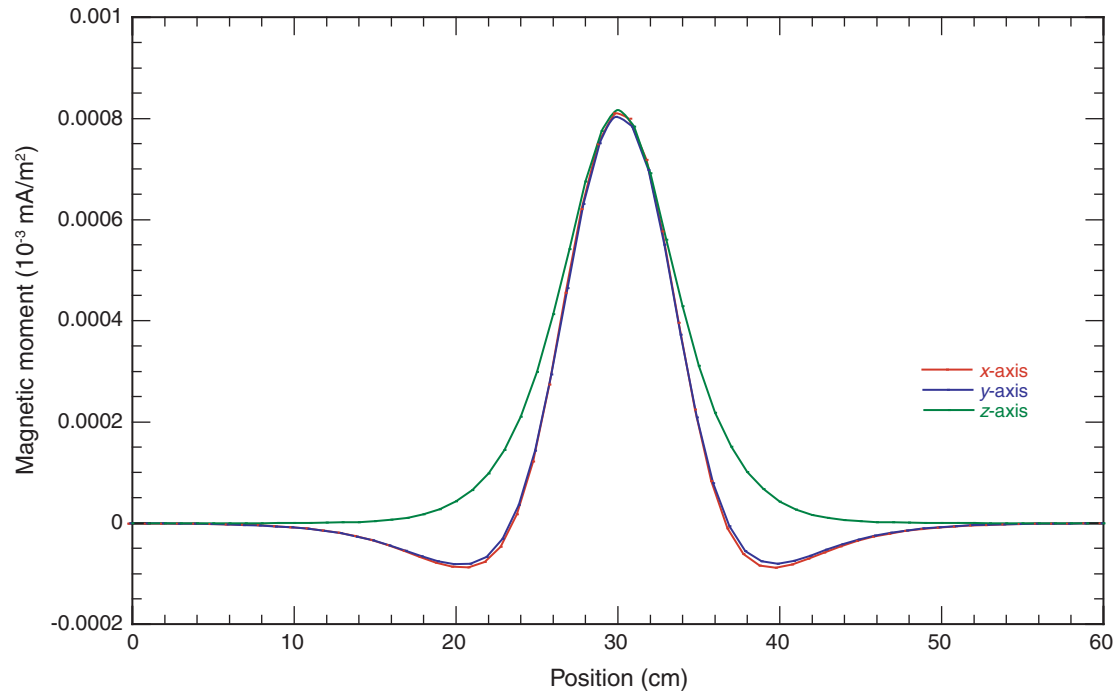
Figure F17. Sensor response of SQUID magnetometer with point source.

Figure F18. Superconducting rock magnetometer coordinates (modified from Richter et al., 2007). SQUID = superconducting quantum interference device.

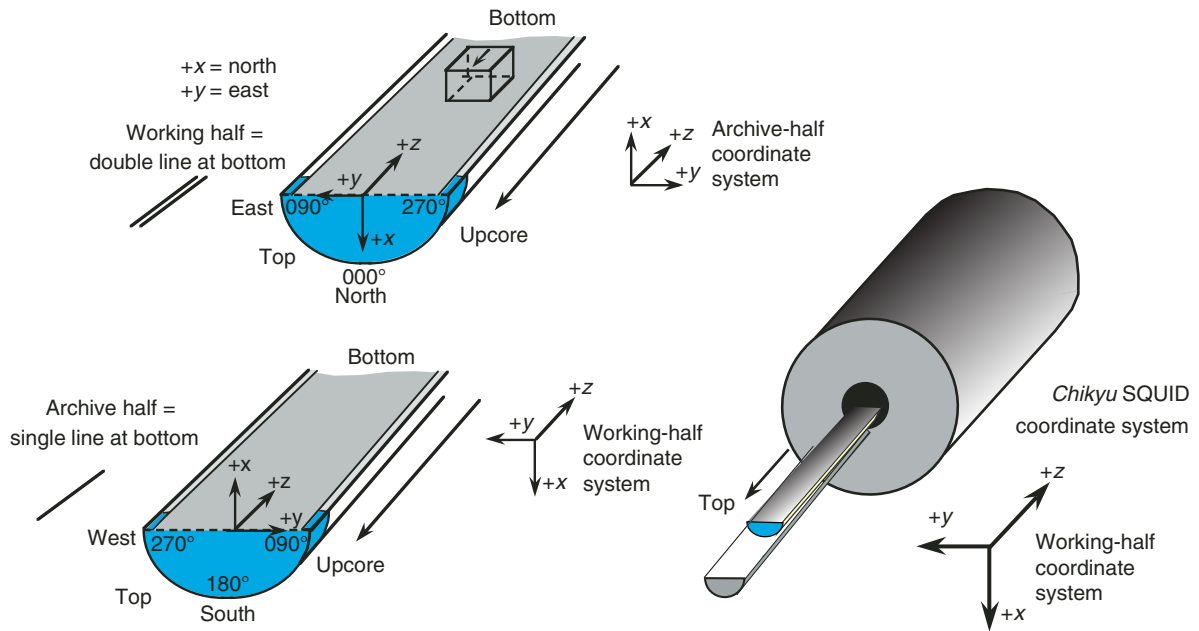


Figure F19. Declination and core twisting (Section 315-C0001F-7H-4). Data correspond to blanket AF demagnetization at 20 mT as obtained in the long-core magnetometer. Note consistent rotation of declination with depth. Such core twisting has been habitually observed in cores obtained with the HPCS.

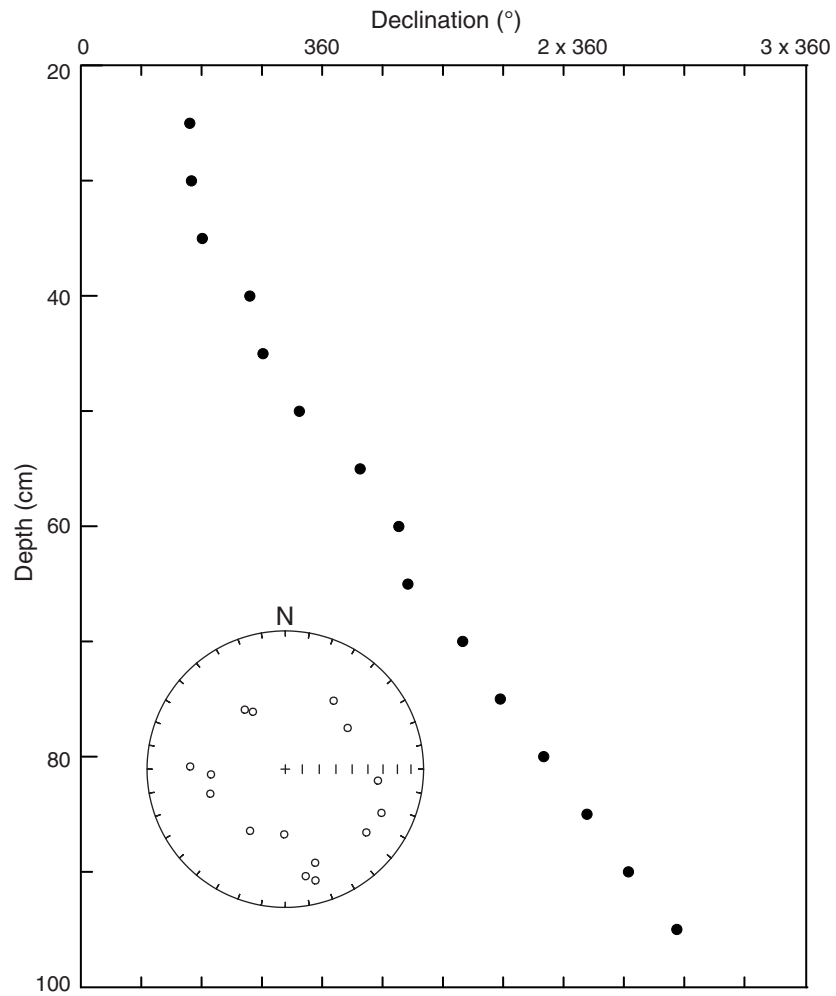


Figure F20. Advanced piston corer temperature tool, third generation (APCT3).



Figure F21. Typical penetration curve consisting of three parts: initial rise of temperature because of frictional heating, decay curve as sensor equilibrates to in situ temperature of sediment, and another rise while tool is pulled out.

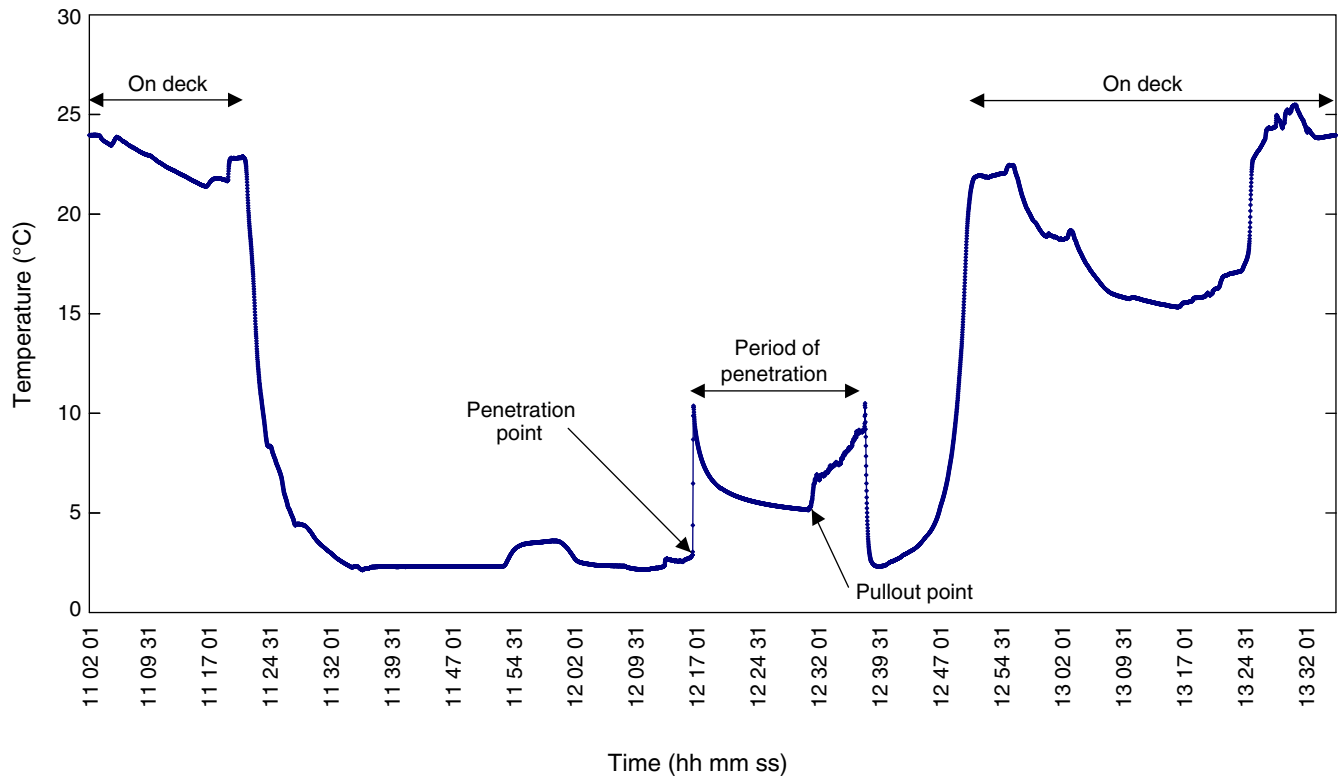
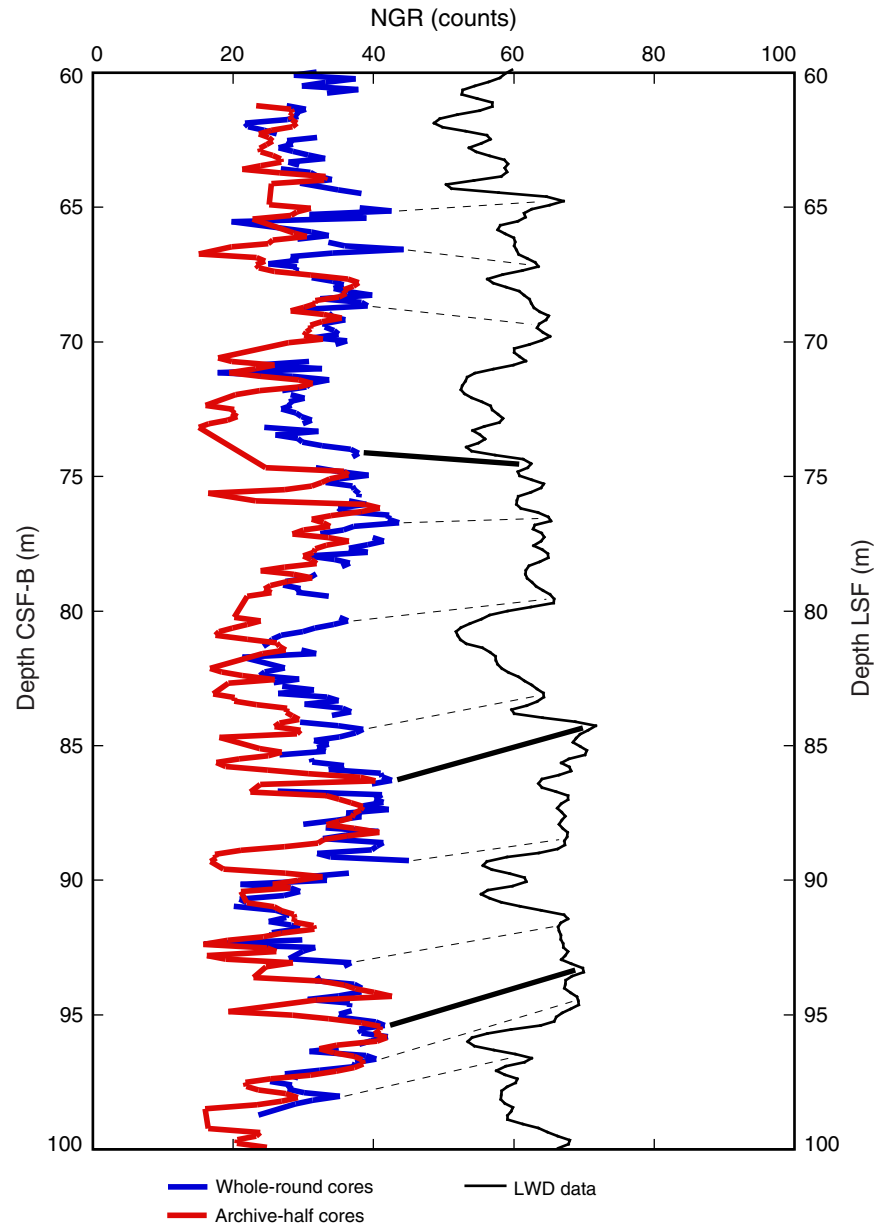
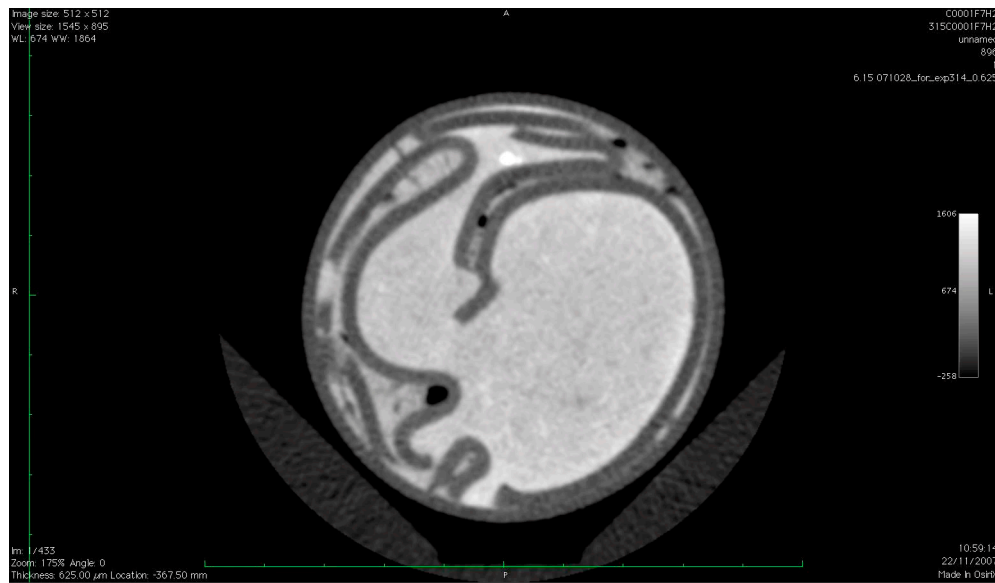


Figure F22. Comparison of natural gamma ray (NGR) activity measurements from MSCL measurements on whole-round and working-half cores and from logging-while-drilling (LWD) GVR tool, Hole C0001E. CSF-B = core depth below seafloor (IODP Method B), LSF = LWD depth below seafloor. Bold lines = correlations defining CSF-B to LSF transfer function, dashed lines = subsidiary correlations.



Movie M1. QuickTime movie of progressive downcore slicing of core damaged by delamination of core liner (Section 315-C0001F-7H-2).



Movie M2. **QuickTime movie** of crosscutting faults imaged in 3-D using OsiriX (Section 315-C0001H-4R-3). Faults appear dark blue. More steeply dipping fault is cut and offset by more shallowly dipping fault.

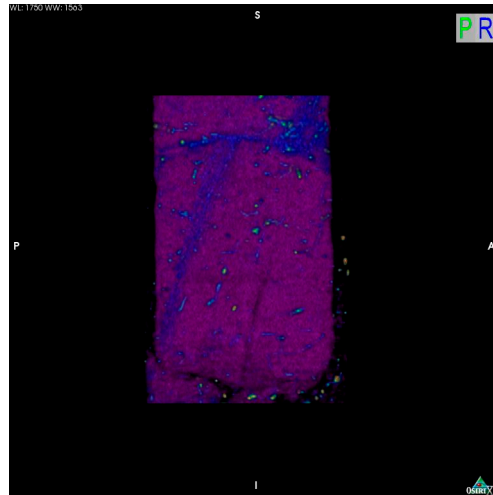


Table T1. Scan settings for X-ray CT scanner. (See table note.)

Setting	Value
Tube voltage (V)	120
Tube current (mA)	100
Source revolution (s)	0.6
Slices per revolution	16
Slice thickness (mm)	0.625
Reconstruction matrix	512 x 512
Pixel size (mm)	0.1876
Field of view (mm ²)	96 x 96
Slice file format	DICOM

Note: DICOM = Digital Imaging and Communication in Medicine.

Table T2. X-ray CT scanner standards. (See table notes.)

Date	Local time (h)	CT number					
		Air	Air SD	Water	Water SD	Aluminum	Aluminum SD
29 Nov 2007	0025	—	—	-1.32	10.30	2476.58	75.93
30 Nov 2007	0140	—	—	1.47	13.27	2487.36	72.51
1 Dec 2007	0035	—	—	-1.51	12.85	2474.02	60.63
2 Dec 2007	0120	—	—	-0.91	12.95	2485.93	72.16
3 Dec 2007	0045	-1006.97	7.18	-1.80	14.68	2464.83	58.96
3 Dec 2007	0411	-1005.18	9.18	-0.56	15.40	2464.34	59.91
4 Dec 2007	0044	-1006.01	7.85	-0.95	13.96	2480.22	68.76
5 Dec 2007	0115	-1006.34	8.03	-2.45	12.59	2457.37	58.27
6 Dec 2007	0035	-1005.99	8.53	-2.43	12.61	2471.55	73.09
6 Dec 2007	2230	-1006.28	7.65	-1.10	14.81	2416.43	66.24
7 Dec 2007	2355	-1006.55	7.32	0.97	13.43	2482.68	51.00
8 Dec 2007	2230	-1006.37	7.98	1.32	13.94	2473.31	65.17
8 Dec 2007	2305	-1006.42	9.45	0.78	12.11	2477.33	60.64
9 Dec 2007	2330	-1007.67	9.42	-1.89	11.27	2477.90	64.79
11 Dec 2007	0530	-1003.81	7.97	2.94	13.27	2471.29	71.91
12 Dec 2007	0330	-1002.25	8.29	1.56	13.36	2480.52	67.64
13 Dec 2007	0025	-1004.16	9.98	2.43	15.73	2471.53	65.62
14 Dec 2007	0150	-1006.17	7.93	1.17	14.30	2469.05	57.42
14 Dec 2007	2127	-1004.81	8.18	5.95	10.35	2464.15	61.73
15 Dec 2007	0220	-1002.44	8.08	3.32	12.82	2488.04	58.74
16 Dec 2007	0305	-1003.41	7.30	3.30	13.98	2466.78	63.24
17 Dec 2007	0320	-1003.48	7.62	2.30	12.85	2483.48	57.90
17 Dec 2007	1905	-1005.27	8.61	0.16	13.91	2486.22	62.75
17 Dec 2007	2233	-1003.26	7.73	5.28	11.65	2484.65	57.73
19 Dec 2007	0105	-1004.91	7.93	2.40	14.53	2473.45	65.36
19 Dec 2007	2240	-1004.20	8.40	2.72	12.82	2491.59	56.61
20 Dec 2007	2125	-1003.65	8.36	-0.62	14.58	2471.07	67.74
22 Dec 2007	0450	-1003.09	8.51	3.43	14.18	2482.15	73.99
23 Dec 2007	0015	-1004.15	7.30	0.57	12.96	2486.75	71.53
23 Dec 2007	2343	-1003.98	9.30	3.85	12.12	2480.02	55.38
24 Dec 2007	2320	-1002.94	7.56	-0.55	13.03	2471.83	60.78
26 Dec 2007	0139	-1004.18	8.01	2.95	12.40	2469.37	63.02
27 Dec 2007	0032	-1003.12	7.30	3.10	12.36	2491.96	74.09
28 Dec 2007	0045	-1003.02	9.37	2.94	14.07	2482.29	51.89
29 Dec 2007	1230	-1003.47	8.30	3.88	12.70	2474.84	61.07
30 Dec 2007	0627	-1003.45	8.62	1.20	13.74	2477.12	64.19
31 Dec 2007	1217	-1003.82	8.46	4.21	14.96	2479.53	65.73
1 Jan 2008	1054	-1003.95	8.11	3.44	13.22	2473.77	64.81
2 Jan 2008	0139	-1003.07	8.56	2.58	14.07	2478.18	61.81
3 Jan 2008	0037	-1003.87	9.90	2.72	14.48	2476.27	73.87
4 Jan 2008	0100	-1004.11	7.81	4.85	12.83	2479.77	73.58
5 Jan 2008	0230	-1003.29	10.44	3.78	12.07	2499.10	65.39
6 Jan 2008	0100	-1003.10	8.77	0.93	14.27	2490.04	63.26
7 Jan 2008	0200	-1003.88	8.93	3.15	11.91	2488.13	54.52
8 Jan 2008	0300	-1003.44	7.87	4.65	11.50	2481.04	69.99
9 Jan 2008	0124	-1004.66	9.26	2.17	13.84	2493.52	58.56
10 Jan 2008	0155	-1002.89	8.98	4.03	13.05	2478.90	59.86
11 Jan 2008	0226	-1003.08	8.45	3.57	12.13	2474.85	76.48
12 Jan 2008	0458	-1003.14	8.72	2.98	11.89	2478.49	61.49
13 Jan 2008	0100	-1002.43	8.67	5.79	15.66	2481.09	58.77
14 Jan 2008	0045	-1003.57	7.41	4.33	11.58	2478.08	69.03
16 Jan 2008	0405	-1004.73	8.65	3.99	13.35	2490.35	66.63
17 Jan 2008	0400	-1003.95	9.75	3.75	12.73	2482.42	61.65
18 Jan 2008	0031	-1003.11	8.80	3.55	12.76	2479.81	54.10
19 Jan 2008	0022	-1002.96	7.91	3.42	12.63	2467.33	65.76
20 Jan 2008	0230	-1004.15	8.33	4.25	12.88	2477.43	58.90
21 Jan 2008	0112	-1004.76	8.90	5.22	12.03	2475.83	61.85
22 Jan 2008	0238	-1004.38	7.73	2.38	15.35	2474.89	64.25
23 Jan 2008	0037	-1002.22	7.96	2.53	15.50	2486.50	62.49
24 Jan 2008	0112	-1004.52	8.57	1.58	12.55	2482.14	67.98
25 Jan 2008	0105	-1002.53	8.32	7.31	13.70	2478.10	68.51
26 Jan 2008	0225	-1003.77	8.69	3.52	14.62	2487.23	60.25
27 Jan 2008	0340	-1002.89	8.75	5.18	11.67	2474.84	66.95
28 Jan 2008	0340	-1002.44	6.27	0.99	13.17	2487.55	70.33
29 Jan 2008	0358	-1003.50	7.11	4.65	12.85	2483.66	65.14
30 Jan 2008	0115	-1003.30	7.58	2.01	14.99	2480.34	62.72
31 Jan 2008	0122	-1003.21	9.15	0.46	12.59	2483.98	71.88

Notes: SD = standard deviation. — = not determined.



Table T3. Characteristic X-ray diffraction peaks for semiquantitative area analysis.

Mineral	Reflection	d-value (Å)	Peak position (°2θ)
Composite clay	Multiple	4.478	19.4–20.4
Quartz	101	3.342	26.3–27.0
Plagioclase	002	3.192	27.4–28.2
Calcite	104	3.035	29.1–29.7

Table T4. Normalization factors for calculation of relative mineral abundance using bulk powder X-ray diffraction analysis. (See table note.)

Affected mineral in standard mixture:	Normalization factors			
	Total clay	Quartz	Plagioclase	Calcite
Influencing mineral:				
Total clay	9.8956702E-03	-1.5889532E-04	-2.8855808E-04	-7.3842803E-04
Quartz	-4.7221169E-05	5.8782392E-04	-4.7869325E-05	-3.1098843E-05
Plagioclase	7.2794763E-04	-4.2840613E-05	1.3719777E-03	-3.6005495E-05
Calcite	4.2042411E-05	3.3021188E-06	-4.1329499E-06	1.3071455E-03

Note: Singular value decomposition was used to compute factors, following Fisher and Underwood (1995).

Table T5. Astrochronological age estimates of nannofossil events used as biostratigraphic tie-points. (See table notes.) (Continued on next page.)

Event	Zone (base)	Age (Ma)
X <i>Gephyrocapsa</i> spp. (>3.5 μm)– <i>Emiliana huxleyi</i>		0.063
FO <i>Emiliana huxleyi</i>	NN21	0.291
LO <i>Pseudoemiliana lacunosa</i>	NN20	0.436
LCO <i>Reticulofenestra asanoi</i>		0.9
RE <i>Gephyrocapsa</i> spp. (≥4 μm)		1.04
FCO <i>Reticulofenestra asanoi</i>		1.078*
LO <i>Gephyrocapsa</i> spp. (>5.5 μm)		1.24
LO <i>Helicosphaera sellii</i>		1.34
FCO <i>Gephyrocapsa</i> spp. (>5.5 μm)		1.46
FO <i>Gephyrocapsa</i> spp. (>5.5 μm)		1.560–1.617*
LO <i>Calcidiscus macintyreii</i> (≥11 μm)		1.6
FO <i>Gephyrocapsa</i> spp. (>3.5 μm)		1.67
LO <i>Discoaster brouweri</i>	NN19	2.06
AB <i>Discoaster triradiatus</i>		2.135–2.216*
LO <i>Discoaster pentaradiatus</i>	NN18	2.393–2.512*
LO <i>Discoaster surculus</i>	NN17	2.52
LO <i>Discoaster tamalis</i>		2.87
LO <i>Sphenolithus</i> spp.		3.65
LO <i>Reticulofenestra pseudoumbilicus</i> (>7 μm)	NN16	3.79
FCO <i>Discoaster asymmetricus</i>	NN15–NN14	4.13
LO <i>Amaurolithus primus</i>		4.5
LO <i>Ceratolithus acutus</i>		5.04
FO <i>Ceratolithus rugosus</i>	NN13	5.12
FO <i>Ceratolithus acutus</i>		5.32
LO <i>Discoaster quinquerramus</i>	NN12	5.59
LO <i>Nicklithus amplificus</i>		5.9*
PE <i>Reticulofenestra pseudoumbilicus</i> (>7 μm)		7.1*
FO <i>Amaurolithus</i> spp. = FO <i>Amaurolithus primus</i>	NN11b	7.362–7.424*
FCO <i>Discoaster surculus</i>		7.88
LCO <i>Minylitha convallis</i>		7.78–8.3*
FO <i>Discoaster berggrenii</i>	NN11a	8.52
PB <i>Reticulofenestra pseudoumbilicus</i>	NN10b	8.785
FO <i>Discoaster pentaradiatus</i>		9.1
LO <i>Catinaster coalitus</i>		9.416
FO <i>Minylitha convallis</i>		9.416
LO <i>Discoaster hamatus</i>	NN10a	9.56
LO <i>Catinaster calyculus</i>		9.687*
X <i>Discoaster hamatus</i> – <i>D. neohamatus</i>		9.762*

Table T5 (continued).

Event	Zone (base)	Age (Ma)
FO <i>Discoaster neohamatus</i>		9.867–10.521*
LCO <i>Discoaster exilis</i>		10.427
FO <i>Discoaster hamatus</i>	NN9	10.541
FO <i>Discoaster calcaris</i>		10.676
FO <i>Discoaster bellus</i> gr.		10.72
FO <i>Discoaster brouweri</i>		10.734–10.764*
FO <i>Catinaster calyculus</i>		10.785
FO <i>Catinaster coalitus</i>	NN8	10.886
LO <i>Coccolithus miopelagicus</i>		10.97–11.02*
LCO <i>Discoaster kugleri</i>		11.578
FCO <i>Discoaster kugleri</i>	NN7	11.863
LO <i>Cyclicargolithus floridanus</i>		12.037
LO <i>Coronocyclus nitescens</i>		12.254
LCO <i>Calcidiscus premacintyreii</i>		12.447
FCO <i>Triquetrorhabdulus rugosus</i>		12.671
LCO <i>Cyclicargolithus floridanus</i>		13.294
LO <i>Sphenolithus heteromorphus</i>	NN6	13.532
LO <i>Helicosphaera ampliaperta</i>	NN5	14.914*
AE <i>Discoaster deflandrei</i>		15.663*
FO <i>Discoaster signus</i>		15.702*
FCO <i>Sphenolithus heteromorphus</i>		17.721*
LCO <i>Sphenolithus belemnus</i>	NN4	17.973*
LO <i>Triquetrorhabdulus carinatus</i>		18.315*
FO <i>Sphenolithus belemnus</i>	NN3	18.921*
FO <i>Helicosphaera ampliaperta</i>		20.393*
X <i>Helicosphaera euphratis</i> – <i>Helicosphaera carteri</i>		20.894*
FCO <i>Helicosphaera carteri</i>		21.985*
LCO <i>Triquetrorhabdulus carinatus</i>		22.092*
FO <i>Sphenolithus disbelemnus</i>		22.760*
FO <i>Discoaster druggi</i>	NN2	22.824*
LO <i>Sphenolithus delphix</i>		23.065*
FO <i>Sphenolithus delphix</i>		23.328*
LO <i>Sphenolithus ciperoensis</i>	NN1	24.242*

Notes: Based on Raffi et al. (2006). X = crossover in abundance, FO = first occurrence, LO = last occurrence, LCO = last consistent occurrence, RE = reentrance, FCO = first consistent occurrence, AB = acme beginning, PB = paracme beginning, PE = paracme end, AE = acme end. * = datum based on Atlantic or Mediterranean records.

Table T6. Planktonic foraminiferal datum events. (See table note.)

Event	Zone (base)	Age (Ma)
LO <i>Globigerinoides ruber rosa</i>		0.12
LO <i>Truncorotalia tosaensis</i>		0.61
FO <i>Truncorotalia crassaformis hessi</i>		0.8
LO <i>Globoturborotalita obliquus</i>		1.3
SD2 <i>Pulleniatina</i> spp.		1.7–1.8
LO <i>Neogloboquadrina asanoi</i>		1.8
FO <i>Truncorotalia truncatulinoides</i>	N.22	1.93
FO <i>Pulleniatina finalis</i>		2.04
FO <i>Globoconella inflata</i> modern form		2.3–2.5
FO <i>Truncorotalia tosaensis</i>	N.21	3.35
LO <i>Dentoglobigerina altispira altispira</i>		3.47
LO <i>Sphaeroidinellopsis seminulina</i>		3.59
LO <i>Hirsutella margaritae</i>		3.85
SD1 <i>Pulleniatina</i> spp.		4.08
FO <i>Truncorotalia crassaformis</i>		4.31
LO <i>Globoturborotalita nepenthes</i>		4.37
FO <i>Globorotalia tumida</i>	N.18	5.57
FO <i>Globigerinoides conglobatus</i>		6.2
FO <i>Pulleniatina primalis</i>	N.17b	6.6
FO <i>Globorotalia plesiotumida</i>	N.17a	8.58
LO <i>Globoquadrina dehiscens</i>		8.5–9.4
FCO <i>Neogloboquadrina acostaensis</i>	N.16	10.57
LO <i>Paragloborotalia mayeri</i>	N.15	11.47
LO <i>Globigerinoides subquadratus</i>		11.54
FO <i>Globoturborotalita nepenthes</i>	N.14	11.63
FO <i>Fohsella lobata</i>	N.12	12.53
FO <i>Fohsella praefohsi</i>	N.11	12.76
FO <i>Fohsella peripheroacuta</i>	N.10	14.24
LO <i>Praeorbulina sicana</i>		14.53
FO <i>Orbulina universa</i>	N.9	14.74
FO <i>Praeorbulina sicana</i>	N.8	16.97
LO <i>Catapsydrax dissimilis</i>	N.7	17.54
FO <i>Globigerinatella insueta</i>	N.6	17.59
LO <i>Paragloborotalia kugleri</i>	N.5	21.12
FO <i>Paragloborotalia kugleri</i>	N.4	22.96

Note: FO = first occurrence, FCO = first consistent occurrence, LO = last occurrence, SD = change in coiling direction from sinistral to dextral.

Table T7. Ages used for the geomagnetic polarity timescale (normal polarity interval). (See table note.)

Age interval (Ma)		Chron/ Subchron	Age interval (Ma)		Chron/ Subchron
Top	Bottom		Top	Bottom	
0.000	0.781	C1n	20.439	20.709	C6An.2n
0.988	1.072	C1r.1n	21.083	21.159	C6AAAn
1.173	1.185	C1r.2n	21.659	21.688	C6AAr.2n
1.778	1.945	C2n	21.767	21.936	C6Bn.1n
2.581	3.032	C2An.1n	21.992	22.268	C6Bn.2n
3.116	3.207	C2An.2n	22.564	22.758	C6Cn.1n
3.330	3.596	C2An.3n	22.902	23.030	C6Cn.2n
4.187	4.300	C3n.1n	23.249	23.375	C6Cn.3n
4.493	4.631	C3n.2n	24.044	24.102	C7n.1n
4.799	4.896	C3n.3n	24.146	24.556	C7n.2n
4.997	5.235	C3n.4n	24.915	25.091	C7An
6.033	6.252	C3An.1n	25.295	25.444	C8n.1n
6.436	6.733	C3An.2n	25.492	26.154	C8n.2n
7.140	7.212	C3Bn	26.714	27.826	C9n
7.251	7.285	C3Br.1n	28.186	28.450	C10n.1n
7.454	7.489	C3Br.2n	28.525	28.715	C10n.2n
7.528	7.642	C4n.1n	29.451	29.740	C11n.1n
7.695	8.108	C4n.2n	29.853	30.217	C11n.2n
8.254	8.300	C4r.1n	30.627	31.116	C12n
8.769	9.098	C4An	33.266	33.738	C13n
9.321	9.409	C4Ar.1n	34.782	35.043	C15n
9.656	9.917	C4Ar.2n	35.404	35.567	C16n.1n
9.779	9.934	C5n.1n	35.707	36.276	C16n.2n
9.987	11.040	C5n.2n	36.512	37.235	C17n.1n
11.118	11.154	C5r.1n	37.345	37.549	C17n.2n
11.554	11.614	C5r.2n	37.610	37.771	C17n.3n
12.041	12.116	C5An.1n	38.032	38.975	C18n.1n
12.207	12.415	C5An.2n	39.041	39.464	C18n.2n
12.730	12.765	C5Ar.1n	40.439	40.671	C19n
12.820	12.878	C5Ar.2n	41.590	42.774	C20n
13.015	13.183	C5AAn	45.346	47.235	C21n
13.252	13.466	C5ABn	48.599	49.427	C22n
13.734	14.095	C5ACn	50.730	50.932	C23n.1n
14.194	14.581	C5ADn	51.057	51.901	C23n.2n
14.784	14.877	C5Bn.1n	52.648	53.004	C24n.1n
15.032	15.160	C5Bn.2n	53.116	53.167	C24n.2n
15.974	16.268	C5Cn.1n	53.286	53.808	C24n.3n
16.303	16.472	C5Cn.2n	56.665	57.180	C25n
16.543	16.721	C5Cn.3n	58.379	58.737	C26n
17.235	17.533	C5Dn	61.650	61.983	C27n
18.056	18.524	C5En	63.104	64.128	C28n
18.748	19.722	C6n	64.432	65.118	C29n
20.040	20.213	C6An.1n			

Note: Data from Gradstein et al. (2004) (See Fig. F16).

Table T8. Modified DSMZ medium 1040. (See table notes.)

Component	Concentration per L	Comments
Sigma sea salts	35 g	
Yeast extract	1 g	
Wolfe's mineral elixir	1 mL	DSMZ medium 792
Resazurin	0.5 mL	1 g/L stock solution
Autoclave, then add the following:		
10% NaHCO ₃	20 mL	
Vitamin solution	1 mL	10 times concentrate of solution described in DSMZ medium 141; mixture of 10 vitamins
FeSO ₄ ·7H ₂ O	5 mL	50 g/L stock solution
Na-dithionate	1 mL	25 g/L stock solution
Substrate	10 mL	1 M stock solution of acetate, lactate, pyruvate, or ethanol

Notes: Adjust pH to 7.2 with H₂SO₄. Concentrations are per liter of Millipore 18.2 MΩ·cm Type 1 ultrapure water.